



**HAL**  
open science

## Adjoint neutron flux calculations with Tripoli-4: Verification and comparison to deterministic codes

N. Terranova, G. Truchet, I. Zmijarevic, A. Zoia

### ► To cite this version:

N. Terranova, G. Truchet, I. Zmijarevic, A. Zoia. Adjoint neutron flux calculations with Tripoli-4: Verification and comparison to deterministic codes. *Annals of Nuclear Energy*, 2018, 114, pp.136-148. 10.1016/j.anucene.2017.12.001 . cea-02421721

**HAL Id: cea-02421721**

**<https://cea.hal.science/cea-02421721>**

Submitted on 20 Dec 2019

**HAL** is a multi-disciplinary open access archive for the deposit and dissemination of scientific research documents, whether they are published or not. The documents may come from teaching and research institutions in France or abroad, or from public or private research centers.

L'archive ouverte pluridisciplinaire **HAL**, est destinée au dépôt et à la diffusion de documents scientifiques de niveau recherche, publiés ou non, émanant des établissements d'enseignement et de recherche français ou étrangers, des laboratoires publics ou privés.

# Adjoint neutron flux calculations with TRIPOLI-4<sup>®</sup>: verification and comparison to deterministic codes

Nicholas Terranova<sup>a</sup>, Guillaume Truchet<sup>b</sup>, Igor Zmijarevic<sup>a</sup>, Andrea Zoia<sup>a,\*</sup>

<sup>a</sup>*Den-Service d'études des réacteurs et de mathématiques appliquées (SERMA), CEA,  
Université Paris-Saclay, F-91191, Gif-sur-Yvette, France*

<sup>b</sup>*CEA, DEN, DER, SPRC, Cadarache, St. Paul-lez-Durance, F-13108, France.*

---

## Abstract

The possibility of computing adjoint-weighted scores by Monte Carlo methods is a subject of active research. In this respect, a major breakthrough has been achieved thanks to the rediscovery of the so-called Iterated Fission Probability (IFP) method, which basically maps the calculation of the adjoint neutron flux into that of the neutron importance function. Based on IFP, we have recently developed the calculation of effective kinetics parameters and sensitivity coefficients to integral reactor responses in the Monte Carlo production code TRIPOLI-4<sup>®</sup>. In view of the next release of the code, we have added a new routine allowing for the calculation of the adjoint angular flux (and more generally adjoint-weighted sources) in eigenvalue problems, which can be useful for code-code comparisons with respect to deterministic solvers. In this work we analyse the behaviour of the adjoint angular flux as a function of space, energy and angle for a few benchmark configurations, ranging from mono-kinetic transport in one-dimensional systems to continuous-energy transport in fuel assemblies. The Monte Carlo adjoint flux profiles are contrasted to reference curves, where available, and to simulation results obtained from ERANOS and APOLLO2 deterministic codes.

*Keywords:* IFP, Monte Carlo, adjoint flux, TRIPOLI-4<sup>®</sup>, Verification and Validation, APOLLO2, ERANOS

---

\*Corresponding author. Tel. +33 (0)1 6908 7976  
Email address: andrea.zoia@cea.fr (Andrea Zoia)

## 1. Introduction

In modern reactor physics, Monte Carlo methods are considered the reference approach to estimate physical quantities to be compared to faster, but approximated, deterministic calculations (Lux and Koblinger, 1991). Extending Monte Carlo codes capabilities to adjoint-weighted scores has attracted intense research efforts in recent years. In principle, computing the adjoint neutron flux would involve the simulation of particles flowing backward from scores to sources, which turns out to be a daunting task (Hoogenboom, 2003).

In this context, the rediscovery of the so-called Iterated Fission Probability (IFP) interpretation of the adjoint flux  $\varphi^\dagger$  (Feghhi et al., 2007, 2008; Nauchi and Kameyama, 2010; Kiedrowski et al., 2011), originally formulated at the beginning of the nuclear era (Soodak, 1949; Weinberg, 1952; Ussachoff, 1955; Hurwitz, 1964), has provided a major breakthrough (Nauchi and Kameyama, 2010; Kiedrowski et al., 2011). In practice, the IFP method allows computing adjoint-weighted scores in  $k$ -eigenvalue problems by formally identifying the neutron importance (which can be obtained in regular forward Monte Carlo simulations) as being proportional to the adjoint neutron flux. A number of production codes have integrated the IFP method, including MCNP (Kiedrowski, 2011), SCALE (Perfetti, 2012), SERPENT (Leppanen, 2014) and TRIPOLI-4<sup>®</sup> (Truchet et al., 2015). By means of IFP, such codes can compute a wide spectrum of adjoint-weighted scores, such as effective kinetics parameters, sensitivity coefficients and first order reactivity perturbations, which can be expressed as ratios of bi-linear functionals of the adjoint and forward flux (Nauchi and Kameyama, 2010; Mosteller and Kiedrowski, 2011; Kiedrowski et al., 2011; Kiedrowski and Brown, 2013; Shim et al., 2011; Truchet, 2014a,b; Leppanen, 2014; Choi and Shim, 2016; Qiu et al., 2016; Zoia and Brun, 2016; Zoia et al., 2016; Terranova and Zoia, 2017).

Among these scores, the adjoint-weighted neutron flux  $\langle \varphi^\dagger, \varphi \rangle$  has been also proposed (Kiedrowski et al., 2011). Comparatively less attention has been devoted to the possibility of explicitly computing the adjoint (angular) neutron flux  $\varphi^\dagger(\mathbf{r}_0, \boldsymbol{\Omega}_0, E_0)$  itself, as a function of position  $\mathbf{r}_0$ , energy  $E_0$  and direction  $\boldsymbol{\Omega}_0$ . This kind of score could be of interest, e.g., for code-to-code comparisons with respect to deterministic solvers, for verification and validation purpose.

In view of a future release of TRIPOLI-4<sup>®</sup>, the production Monte Carlo code developed at CEA (Brun et al., 2015), we have revisited the adjoint flux calculation routines that had been originally implemented in a development version of the code (Truchet, 2015). A special simulation mode has been developed in order to estimate scalar products of the kind  $\langle \varphi^\dagger, S \rangle$ , where  $S$  is an arbitrary user-defined source. The scalar products are then decomposed on a spatial, en-

ergetic and angular mesh with respect to the initial coordinates of the neutrons. In particular, by taking a delta-like source  $S = \delta(\mathbf{r} - \mathbf{r}_0)\delta(\boldsymbol{\Omega} - \boldsymbol{\Omega}_0)\delta(E - E_0)$  at a given point of the phase space, the scalar product precisely defines the adjoint flux  $\varphi^\dagger(\mathbf{r}_0, \boldsymbol{\Omega}_0, E_0)$ .

In this paper, we illustrate the application of the IFP method in TRIPOLI-4<sup>®</sup> for adjoint flux calculations. For this purpose, verification cases will be discussed, and the adjoint flux shapes obtained by Monte Carlo methods will be compared to reference solutions (where available) and to the results of deterministic solvers. For these latter, we will use the codes ERANOS (Ruggieri et al., 2006) and APOLL02 (Sanchez et al., 1988, 2010). This manuscript is organized as follows: in Sec. 2 we will briefly recall the theoretical background of the IFP method (in order for this manuscript to be self-contained), and we will detail the algorithm implemented in TRIPOLI-4<sup>®</sup> to estimate the adjoint flux. In Secs. 3 and 4 we will then illustrate a few significant verification tests for mono-kinetic transport, two-group transport and continuous-energy transport in one-dimensional systems, sodium-cooled fuel pin-cells, and PWR fuel assemblies. Then, in Sec. 5 we will discuss in detail spatial and spectral effects for the case of UOX and MOX assemblies, and in Sec. 6 we will examine the performances of the IFP algorithm for the adjoint flux as compared to regular forward calculations for  $k$ -eigenvalue problems. Conclusions will be finally drawn in Sec. 7.

## 2. The IFP method

In this section we will briefly recall the theoretical background of the IFP method, by basically following the derivation proposed in (Nauchi and Kameyama, 2010).

### 2.1. The adjoint transport equation

The critical  $k$ -eigenvalue Boltzmann equation for the neutron flux eigenfunctions  $\varphi_k(\mathbf{r}, \mathbf{v})$  can be written in operator notation (Bell and Glasstone, 1970)

$$L \varphi_k(\mathbf{r}, \mathbf{v}) = \frac{1}{k} F \varphi_k(\mathbf{r}, \mathbf{v}), \quad (1)$$

where the net disappearance operator  $L$  and the fission operator  $F$  are respectively defined as

$$L f = \boldsymbol{\Omega} \cdot \nabla f + \Sigma_t f - \int \Sigma_s(\mathbf{r}, \mathbf{v}' \rightarrow \mathbf{v}) f(\mathbf{r}, \mathbf{v}') d\mathbf{v}', \quad (2)$$

$$F f = \frac{1}{4\pi} \int \nu(v') \Sigma_f(\mathbf{r}, \mathbf{v}') \chi(\mathbf{r}, v' \rightarrow v) f(\mathbf{r}, \mathbf{v}') d\mathbf{v}'. \quad (3)$$

70 Introducing the Dirac notation, the inner product between any two square-integrable functionals  $\varphi$  and  $\varphi^\dagger$ , defined in the  $\{\mathbf{r}, \mathbf{v}\}$  phase space, can be expressed as

$$\langle \varphi^\dagger, \varphi \rangle = \int_{\{\mathbf{r}, \mathbf{v}\}} \varphi^\dagger(\mathbf{r}, \mathbf{v}) \varphi(\mathbf{r}, \mathbf{v}) d\mathbf{r} d\mathbf{v} \quad (4)$$

Under suitable continuity and boundary conditions (Bell and Glasstone, 1970; Henry, 1975), an adjoint operator  $A^\dagger$  can be defined for the operator  $A$  such that

$$\langle \varphi^\dagger, A \varphi \rangle = \langle \varphi, A^\dagger \varphi^\dagger \rangle. \quad (5)$$

The adjoint eigenvalue transport equation reads then

$$L^\dagger \varphi_k^\dagger(\mathbf{r}, \mathbf{v}) = \frac{1}{k^\dagger} F^\dagger \varphi_k^\dagger(\mathbf{r}, \mathbf{v}), \quad (6)$$

75 where

$$L^\dagger f = -\boldsymbol{\Omega} \cdot \nabla f + \Sigma_t f - \int \Sigma_s(\mathbf{r}, \mathbf{v} \rightarrow \mathbf{v}') f(\mathbf{r}, \mathbf{v}') d\mathbf{v}', \quad (7)$$

and

$$F^\dagger f = \frac{1}{4\pi} \int \nu(v) \Sigma_f(\mathbf{r}, \mathbf{v}) \chi(\mathbf{r}, v \rightarrow v') f(\mathbf{r}, \mathbf{v}') d\mathbf{v}'. \quad (8)$$

The fundamental mode of the adjoint transport equation,  $\varphi_0^\dagger$  is known as the adjoint flux, with associated eigenvalue  $k_0^\dagger = k_0$  equal to the fundamental forward eigenvalue.

## 80 2.2. Relation between IFP and adjoint equations

The physical interpretation of  $\varphi_0^\dagger$  is usually established by formally equating Eq. (6) with the backward equation for the neutron importance, up to an arbitrary normalization constant (Soodak, 1949; Weinberg, 1952; Ussachoff, 1955; Hurwitz, 1964). In a multiplying system, the neutron importance  $I(\mathbf{r}, \mathbf{v})$  is defined as the average number of descendant neutrons produced asymptotically in a distant generation by a single neutron initially injected at phase space coordinates  $(\mathbf{r}, \mathbf{v})$  (Ussachoff, 1955; Henry, 1975). The neutron importance can be shown to satisfy the backward balance equation (Ussachoff, 1955; Nauchi and Kameyama, 2010)

$$0 = \boldsymbol{\Omega} \cdot \nabla I(\mathbf{r}, \mathbf{v}) - \Sigma_t I(\mathbf{r}, \mathbf{v}) + \int d\mathbf{v}' \Sigma_s(\mathbf{r}, \mathbf{v} \rightarrow \mathbf{v}') I(\mathbf{r}, \mathbf{v}') + \frac{\nu_t \Sigma_f(\mathbf{r}, v)}{4\pi k} \int d\mathbf{v}' \chi_t(v \rightarrow v') I(\mathbf{r}, \mathbf{v}'). \quad (9)$$

By inspection, the neutron importance  $I(\mathbf{r}, \mathbf{v})$  turns out to be proportional to the adjoint flux  $\varphi^\dagger(\mathbf{r}, \mathbf{v})$ , solution of the eigenvalue adjoint neutron transport equation given in Eq. (6).

### 2.3. The IFP algorithm for the adjoint flux

85 The formal identification between the neutron importance and the adjoint flux lies at the basis of the so-called Iterated Fission Probability method (Feghhi et al., 2007, 2008; Nauchi and Kameyama, 2010; Kiedrowski et al., 2011). In order to compute the importance function  $I(\mathbf{r}_0, \mathbf{v}_0)$ , and thus estimate the adjoint neutron flux for multiplying systems, we have implemented a new simulation mode  
 90 in the production Monte Carlo TRIPOLI-4<sup>®</sup>. In practice, the quantity  $I(\mathbf{r}_0, \mathbf{v}_0)$  is estimated by running an ensemble of  $B$  fixed-source replicas (batches) over  $M$  fission generations (see Fig. 1). For each batch,  $N$  neutrons start with coordinates  $\mathbf{r}_0, \mathbf{v}_0$ . The quantity  $M$  defines the IFP cycle length. If  $M$  is sufficiently large, the neutron population  $(\pi)_i$  descending from a common ancestor  $i$  reaches  
 95 an asymptotic distribution, and the importance  $I_k$  at generation  $M$  can be thus obtained by collecting the simulation weights of all fission neutrons at generation  $M + 1$  descending from their common ancestors. To prevent the neutron population from exploding or going to extinction over the  $M$  latent generations, a rescaling factor equal to  $1/k^{(g)}$  (the multiplication factor estimated at the latent  
 100 generation  $g$ ) is applied. The quantity  $k^{(g)}$  asymptotically converges to the fundamental  $k$ -eigenvalue for a sufficiently large cycle length  $M$ , and the associated importance yields the fundamental adjoint neutron flux  $\varphi_0^\dagger(\mathbf{r}_0, \mathbf{v}_0)$  evaluated at the phase space coordinates where the ancestor neutron has been injected (up to a normalization factor).

105 Actually, the algorithm implemented in TRIPOLI-4<sup>®</sup> allows more generally computing scalar products of the kind  $\langle \varphi^\dagger, S \rangle$ , where  $S$  is an arbitrary user-defined source, and then decomposing the resulting scores on a spatial, energetic and angular mesh with respect to the starting coordinates of the neutrons. As a particular case, for delta-like sources at a given point in phase space we recover  
 110 the adjoint flux  $\varphi_0^\dagger(\mathbf{r}_0, \mathbf{v}_0)$ .

### 2.4. Determining the IFP cycle length

Selecting a proper IFP cycle length  $M$  for IFP simulations might be a difficult task (Nauchi and Kameyama, 2010; Kiedrowski et al., 2011). Longer cycles ensure a better convergence to the asymptotic behaviour, thus minimizing the  
 115 approximation due to a finite number of IFP generations. On the other hand, for excessively long cycles neutron histories might be killed before contributing to the final score, thus increasing the variance of the calculation. In order to

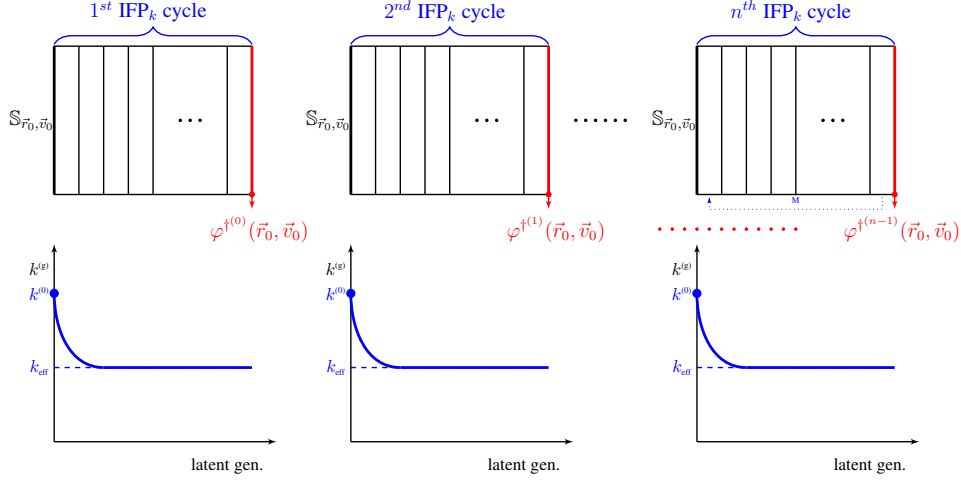


Figure 1: The IFP method as applied to the calculation of the adjoint flux.

provide a convergence estimator for the IFP scores, we have implemented in TRIPOLI-4<sup>®</sup> the so-called relative information entropy between two cycle lengths. The relative entropy, also known as the Kullback-Leibler divergence (Cover and Thomas , 2006), provides a measure of the distance between two distributions. For two discrete probability distributions  $p$  and  $q$ , the relative entropy is defined as (Shannon , 1948; Cover and Thomas , 2006)

$$D(p||q) = \sum_j p(j) \log \frac{p(j)}{q(j)}. \quad (10)$$

Roughly speaking, the relative entropy  $D(p||q)$  quantifies the approximation that we make by taking  $q(x)$  as a probability distribution, whereas the true distribution is  $p(x)$ . The idea is that we can assume as a reference distribution the one which is obtained taking the longest cycle length  $M$ . This definition could be then applied to the different adjoint scores distributions  $\pi_i^M$  and  $\pi_i^{M'}$  for the generic phase-space score bin  $x_i$ , associated to two different cycle lengths  $M' < M$  (Truchet, 2015):

$$p(x_i) = \frac{\pi_i^M}{\sum_j \pi_j^M} \quad (11)$$

$$q(x_i) = \frac{\pi_i^{M'}}{\sum_j \pi_j^{M'}}. \quad (12)$$

The following relative entropy for the two cycles can be estimated:

$$D(p||q) = \sum_i \frac{\pi_i^M}{\sum_j \pi_j^M} \log \left( \frac{\sum_j \pi_j^{M'} \pi_i^M}{\pi_i^{M'} \sum_j \pi_j^M} \right) \quad (13)$$

$$= \log \left( \sum_j \pi_j^{M'} \right) - \log \left( \sum_j \pi_j^M \right) + \frac{\sum_j \pi_j^{M'} \log \frac{\pi_j^M}{\pi_j^{M'}}}{\sum_j \pi_j^M}. \quad (14)$$

In the following, the simulation results for the Kullback-Leibler divergence will be normalized to the absolute entropy of the longest cycle  $M$ , defined as (Shannon , 1948)

$$H(p) = \sum_x p(x) \log \frac{1}{p(x)} \quad (15)$$

$$= \log \left( \sum_i \pi_i^M \right) - \frac{\sum_i \pi_i^M \log \pi_i^M}{\sum_i \pi_i^M}. \quad (16)$$

As shown in the next Sections, the  $D(p||q)$  measure has been used in the verification test cases in order to determine the relative entropy for different cycle lengths  $M$  and get some insight on the convergence of the IFP algorithm for different reactor configurations.

### 3. Verification on simple multiplying systems

In this section we will illustrate some examples of verification tests for the adjoint flux calculations that have been realized by using TRIPOLI-4<sup>®</sup>.

#### 3.1. Two-group, infinite medium transport

As a first application, let us consider a homogeneous system of infinite size, with two energy groups  $v_1$  (fast) and  $v_2$  (thermal) and two delayed families  $a$  and  $b$ . We assume, as in (Kiedrowski, 2010), that no up-scattering is possible, fissions can be induced only by neutrons colliding in the thermal group  $g = 2$  and finally fission neutrons are emitted exclusively in  $g = 1$ . Under such conditions, the  $k$ -eigenvalue transport problem can be reduced to a system of equations for the scalar flux  $\varphi$ , namely,

$$\begin{aligned} \Sigma_{r,1} \varphi_{k,1} &= \frac{1}{k} (1 - \beta_{\text{tot}} + \xi_1) \nu_{f,2} \Sigma_{f,2} \varphi_{k,2} \\ \Sigma_{r,2} \varphi_{k,2} &= \Sigma_{s,12} \varphi_{k,1} + \frac{1}{k} \xi_2 \nu_{f,2} \Sigma_{f,2} \varphi_{k,2}, \end{aligned} \quad (17)$$

$g$	$\Sigma_{rg}$	$\Sigma_{fg}$	$\chi_{a \rightarrow g}$	$\chi_{b \rightarrow g}$	$\Sigma_{s,g \rightarrow 1}$	$\Sigma_{s,g \rightarrow 2}$	$\Sigma_{ag}$
1	1.5	0	3/4	1/2	1/2	1/2	1
2	2	1	1/4	1/2	0	1	1.5

Table 1: The physical parameters for the two-group infinite medium system, expressed in arbitrary units.

where  $\varphi_{k,g} = \varphi_k(v_g)$  and  $\Sigma_{x,g} = \Sigma_x(v_g)$ . Here  $\Sigma_{s,gj} = \Sigma_s(v_g \rightarrow v_j)$  is the differential scattering kernel,  $\Sigma_{r,g} = \Sigma_{r,g} - \Sigma_{s,gg}$  the removal cross-section of group  $g$ ,  $\Sigma_{f,g}$  the fission cross-section of group  $g$ ,  $\nu_{f,g}$  the number of neutrons produced by a fission in group  $g$ ,  $\chi_{i,g}$  is the delayed neutron spectrum from delayed family  $i$  to energy group  $g$ ,  $\beta_i$  the delayed neutron fraction of family  $i$ ,  $\beta_{\text{tot}} = \beta_a + \beta_b$ , and  $\xi_g = \chi_{a,g}\beta_a + \chi_{b,g}\beta_b$ . The associated adjoint equations can be obtained from Eqs. (17) by transposition, i.e.,

$$\begin{aligned}\Sigma_{r,1}\varphi_{k,1}^\dagger &= \Sigma_{s,12}\varphi_{k,2}^\dagger \\ \Sigma_{r,2}\varphi_{k,2}^\dagger &= \frac{1}{k} \left[ (1 - \beta + \xi_1)\nu_{f,2}\Sigma_{f,2}\varphi_{k,1}^\dagger + \xi_2\nu_{f,2}\Sigma_{f,2}\varphi_{k,2}^\dagger \right].\end{aligned}\quad (18)$$

For this simple configuration, it is possible to derive analytical solutions for the forward flux ratio (Kiedrowski, 2010)

$$z = \frac{\varphi_2}{\varphi_1} = \frac{\Sigma_{s,12}}{\Sigma_{r,2} - \frac{1}{k_{\text{eff}}}\xi_2\nu_{f,2}\Sigma_{f,2}},\quad (19)$$

and the adjoint flux ratio

$$z^\dagger = \frac{\varphi_1^\dagger}{\varphi_2^\dagger} = \frac{\Sigma_{s,12}}{\Sigma_{r,1}},\quad (20)$$

as well as the multiplication factor

$$k = \frac{\nu_{f,2}\Sigma_{f,2}}{\Sigma_{r,2}} \left[ z^\dagger(1 - \beta + \xi_1) + \xi_2 \right].\quad (21)$$

The physical parameters chosen for our simulations are reported in Tab. 1.

The TRIPOLI-4<sup>®</sup> scattering and fission kernels were modified to meet the specifications of the simplified model. In Fig. 2 the adjoint flux ratio  $\varphi_1^\dagger/\varphi_2^\dagger$  is provided as a function of the absorption cross section of the first (fast) group. For the Monte Carlo calculations,  $10^4$  neutrons were simulated in  $10^3$  cycles.

For verification purposes, an IFP cycle length of  $M = 10$  was chosen, wven if lower values were largely sufficient to achieve the convergence of the importance for this a simple configuration. The 2-group TRIPOLI-4<sup>®</sup> results with a  $2\text{-}\sigma$  error bar<sup>1</sup> have been compared to the exact solutions given in Eq. (20), showing a good agreement.

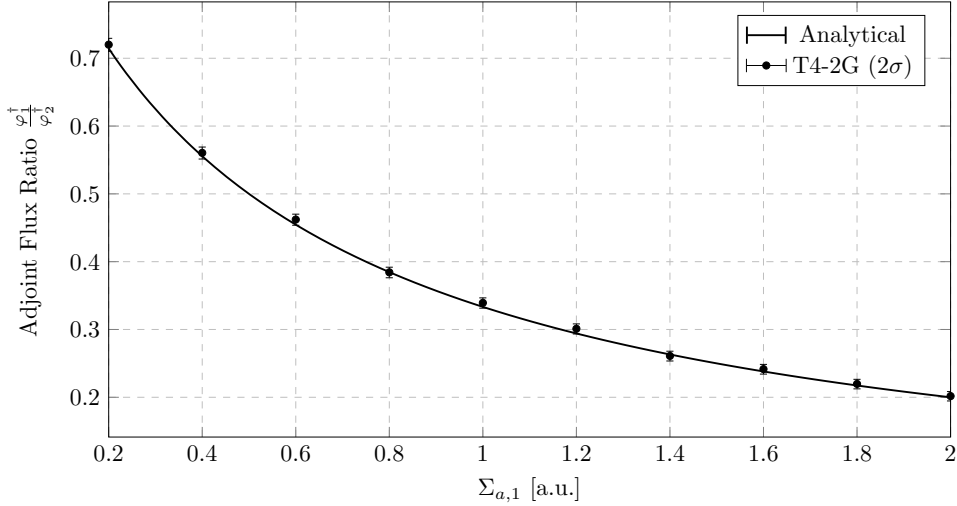


Figure 2: Comparison between TRIPOLI-4<sup>®</sup> calculations and exact solutions for the adjoint flux ratio as a function of the absorption cross section in the first group  $\Sigma_{a,1}$ .

### 3.2. Mono-kinetic transport

As a second application we compute the adjoint neutron flux for mono-kinetic transport. In this case, the forward and adjoint scalar fluxes are identical, while the angular fluxes are equal for opposite directions, namely,

$$\varphi(\mathbf{\Omega}) = \varphi^\dagger(-\mathbf{\Omega}). \quad (23)$$

This property has been conveniently used in order to verify the IFP method implemented in TRIPOLI-4<sup>®</sup>.

<sup>1</sup>TRIPOLI-4<sup>®</sup> can provide the adjoint flux for each group. The standard deviation for the ratio between two groups has been derived by using

$$\sigma\left(\frac{\varphi_1^\dagger}{\varphi_2^\dagger}\right) \approx \sqrt{\left[\frac{1}{\varphi_2^\dagger}\sigma(\varphi_1^\dagger)\right]^2 + \left[\frac{\varphi_1^\dagger}{\varphi_2^{\dagger,2}}\sigma(\varphi_2^\dagger)\right]^2}. \quad (22)$$

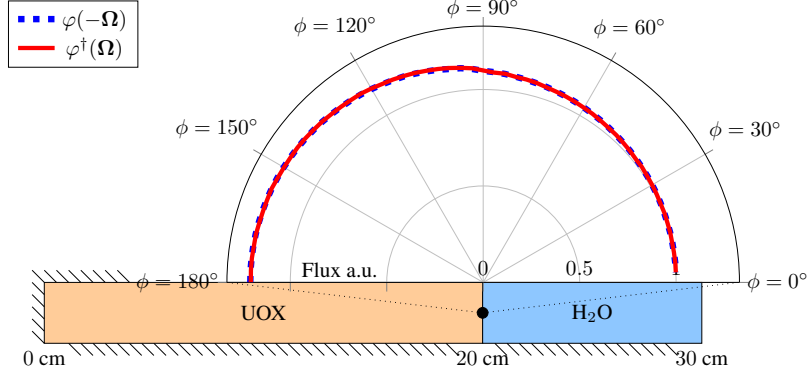


Figure 3: Comparison between the forward and the adjoint angular flux in opposite directions, for a mono-kinetic calculation. Results are given in arbitrary units.

The reactor configuration consists of two adjacent boxes, the former filled with fuel and the latter filled with water (see Fig. 3). Reflecting boundary conditions have been imposed on the faces whose normal vectors are aligned along  $-\mathbf{x}$ ,  $\pm\mathbf{y}$  and  $\pm\mathbf{z}$  directions. Vacuum boundaries are imposed along the  $+\mathbf{x}$  direction. The angular flux has been computed at the interface between fuel and water.

In Fig. 3 we display the comparison between the forward and the adjoint azimuthal flux for opposite directions<sup>2</sup>. The simulation results show a good agreement between the two calculations performed by TRIPOLI-4<sup>®</sup>, which is coherent with Eq. 23. A total of  $10^5$  neutrons and  $10^5$  batches have been used for both forward and adjoint simulations. For the adjoint flux, an IFP cycle length of  $M = 6$  latent generations has been chosen. This value is to be compared with the relative entropy plot presented in Fig. 4. As mentioned in the previous section, the Kullback-Leibler factor  $D$  has been computed by taking as reference cycle length  $M_{max} = 8$ , which was deemed to be sufficient for this simple configuration.

<sup>2</sup>Supposing the angular distribution described by two angles  $\phi$  and  $\theta$ , we show the angular forward and adjoint flux integrated over  $\theta$  for opposite  $\phi$  angles.

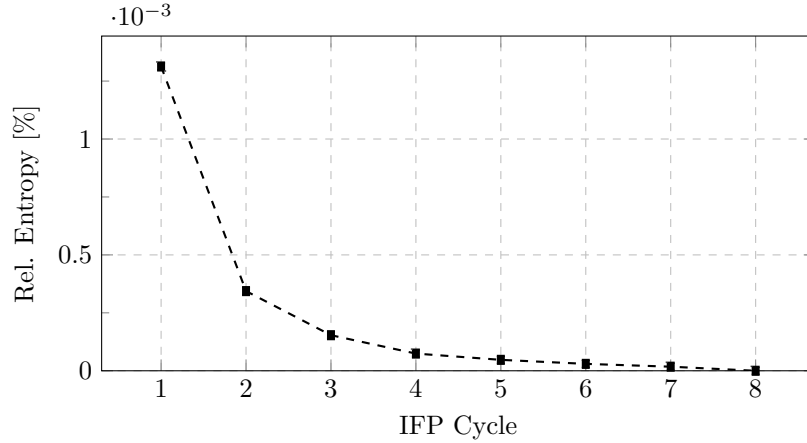


Figure 4: Relative entropy calculation for the mono-kinetic reactor configuration, by assuming  $M_{max} = 8$ .

#### 4. Analysis of reactor configurations

A few realistic reactor configurations have been selected in order to probe the behaviour of the adjoint flux computed by TRIPOLI-4<sup>®</sup> with respect to the results obtained from deterministic solvers. For each reactor test case, geometrical and material specifications are provided in order to ensure benchmark-quality results.

##### 4.1. Simplified SFR reactor

As a first configuration, we have examined the 2D axial section of a Sodium-cooled Fast Reactor (SFR) (Truchet, 2014b). The reactor geometry is provided in Fig. 5 and the compositions are given in Tab. 2. The geometry is basically made of several layers of different materials, with leakage boundary conditions on the axial direction.

The adjoint neutron flux  $\varphi^\dagger(E)$  averaged on the whole geometry and computed by using TRIPOLI-4<sup>®</sup> is illustrated in Fig. 6. The Monte Carlo simulation results obtained with  $3 \times 10^6$  neutrons and  $5 \times 10^4$  cycles are compared to those of the deterministic solver ERANOS/BISTRO (Ruggieri et al., 2006) using a 1968 energy group mesh with a P3 anisotropy order. The ERANOS code<sup>3</sup> is a reactor physics calculation system including various deterministic solvers for the neutron transport equation, developed and validated for current and advanced fast spectrum reactor applications. In particular, the ERANOS/BISTRO

<sup>3</sup>European Reactor ANalysis Optimized calculation System.

	Composition $\frac{10^{24}}{\text{cm}^3}$		Composition $\frac{10^{24}}{\text{cm}^3}$
<b>Top Reflector</b>			
$^{52}\text{Cr}$	1.319373E-2	$^{56}\text{Fe}$	4.875390E-2
$^{58}\text{Ni}$	4.883710E-3	$^{60}\text{Ni}$	1.895516E-3
<b>Blanket</b>			
$^{238}\text{U}$	1.405553E-2	$^{16}\text{O}$	2.818029E-2
$^{27}\text{Al}$	4.443492E-3	$^{52}\text{Cr}$	1.127610E-3
$^{56}\text{Fe}$	4.155072E-3	$^{58}\text{Ni}$	4.161906E-4
$^{60}\text{Ni}$	1.619658E-4		
<b>Plenum</b>			
$^{52}\text{Cr}$	2.350464E-3	$^{56}\text{Fe}$	8.673668E-3
$^{58}\text{Ni}$	8.687959E-4	$^{60}\text{Ni}$	3.379375E-4
<b>Fuel1-2-3</b>			
$^{239}\text{Pu}$	1.067352E-3	$^{52}\text{Cr}$	1.779916E-3
$^{56}\text{Fe}$	6.548571E-3	$^{58}\text{Ni}$	6.520389E-4
$^{60}\text{Ni}$	2.537198E-4	$^{238}\text{U}$	7.871417E-3
$^{16}\text{O}$	1.578161E-2	$^{27}\text{Al}$	2.488458E-3
$^{23}\text{Na}$	6.229042E-9		
<b>Bottom Reflector</b>			
$^{52}\text{Cr}$	1.127610E-3	$^{56}\text{Fe}$	4.155072E-3
$^{58}\text{Ni}$	4.161906E-4	$^{60}\text{Ni}$	1.619658E-4

Table 2: Material compositions of the simplified SFR geometry shown in Fig. 5.

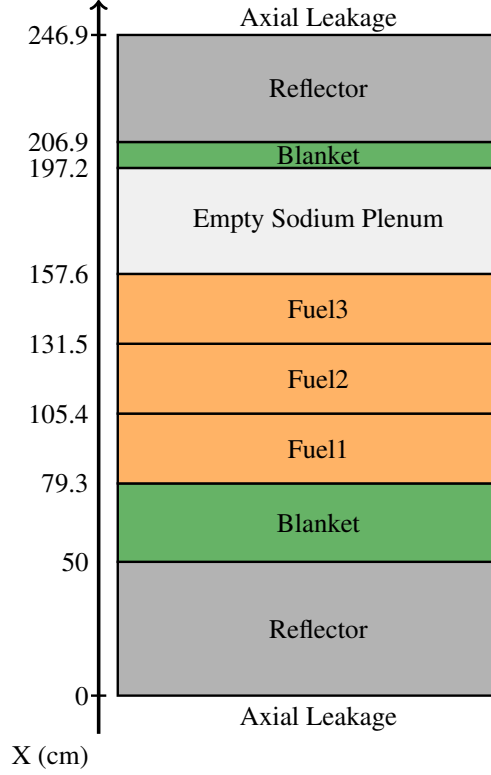


Figure 5: 1D axial section of the Sodium-cooled Fast Reactor (SFR) configuration.

solver (Palmiotti et al. , 1990) allows finite difference Sn transport calculations with an improved convergence algorithm, which can be used in 1D and 2D geometries.

185 The adjoint flux computed with TRIPOLI-4<sup>®</sup> has been decomposed on an energy mesh exactly matching that of ERANOS/BISTRO. Spatial and angular variables have been averaged out. For the Monte Carlo results,  $1\sigma$  error bars are also displayed, barely visible in the top part of the figure. For the SFR configuration tested here, TRIPOLI-4<sup>®</sup> and ERANOS provide consistent results over the whole  
 190 energy range. This is confirmed by the reduced  $\chi^2$  test, defined as

$$\chi^2 = \frac{1}{(G-1)} \sum_{g=1}^G \frac{(\varphi_{g,T4}^\dagger - \varphi_{g,det}^\dagger)^2}{\sigma_{g,T4}^2}, \quad (24)$$

where the sum is extended over the the number of energy groups  $G$ ,  $\varphi_{g,det}^\dagger$  is the deterministic value for group  $g$ , and  $\varphi_{g,T4}^\dagger$  the TRIPOLI-4<sup>®</sup> adjoint flux score

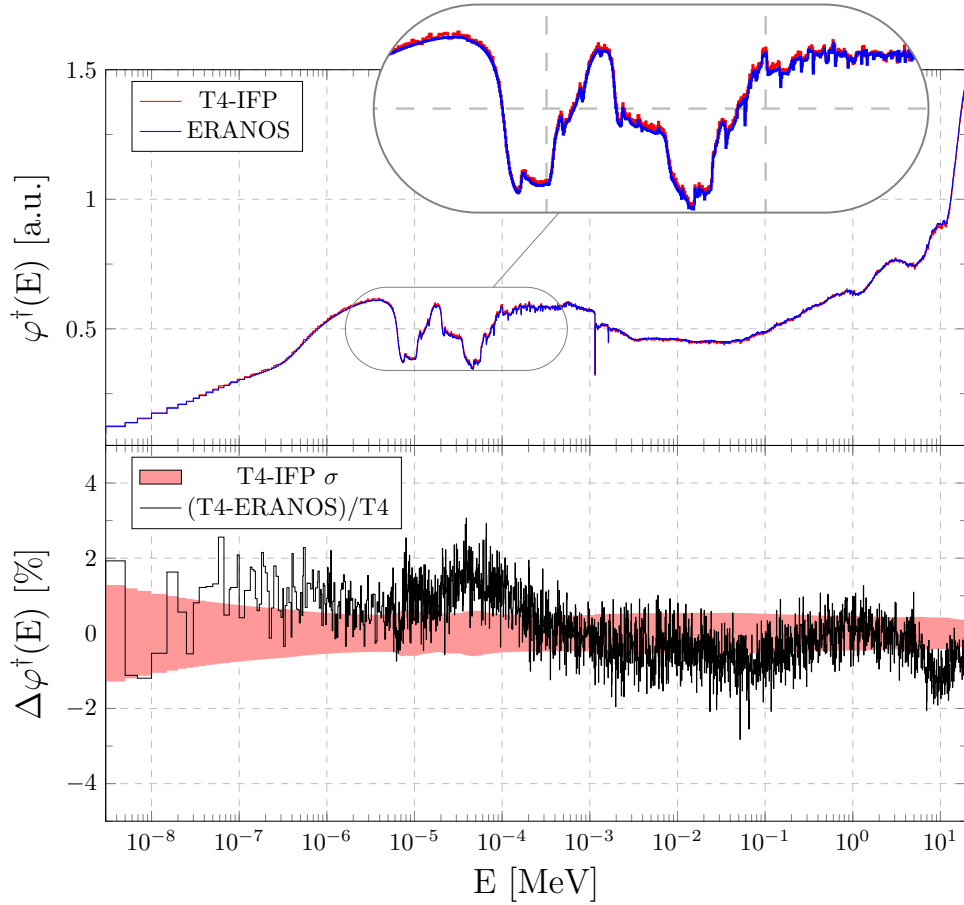


Figure 6: Comparison between ERANOS and TRIPOLI-4<sup>®</sup> adjoint flux calculations for an SFR-like simplified reactor with empty sodium plenum (top). Relative differences between TRIPOLI-4<sup>®</sup> and ERANOS are checked against the Monte Carlo  $1\sigma$ -error bars (bottom).

(with associated standard deviation  $\sigma_{g,T4}$ ). For our simulations, we have obtained  $\chi^2 \simeq 2.8$  which is a satisfactory result<sup>4</sup>.

195 Note that TRIPOLI-4<sup>®</sup> results are obtained by using continuous-energy particle transport, which could explain the slight differences observed. Moreover, in ERANOS the cross section self-shielding procedure used to solve the adjoint transport equation is based on the forward flux. This could be responsible of

<sup>4</sup>A perfect agreement is achieved when the reduced  $\chi^2$  test provides a result of 1. However, the two quantities for which the cost function  $\chi^2$  is calculated are two adjoint fluxes obtained by different numerical tools. A value of 2.8 could be considered a quite satisfactory result if we consider all the approximations introduced in the deterministic solvers.

some deviations visible in the energy range corresponding to resonances. This  
200 phenomenon is expected to worsen when larger energy meshes are adopted in  
the deterministic solvers, as shown in the following.

#### 4.2. Sodium-cooled MOX fuel pin-cell

As a second configuration, we have considered a sodium-cooled MOX fuel  
pin-cell, whose geometry and material compositions are illustrated in Fig. 7 and  
205 Tab. 3, respectively. The adjoint neutron flux  $\varphi^\dagger(E)$  computed by TRIPOLI-4<sup>®</sup>  
is shown in Fig. 8: the Monte Carlo results are compared to those obtained  
with the deterministic code APOLL02 using a Method of Characteristics (MOC)  
solver (Sanchez et al., 1988, 2010). The APOLL02 spectral transport code al-  
lows cross section generation, forward and adjoint transport calculations through  
210 several deterministic solvers, i.e., collision probability method, nodal Sn and  
short/long MOC. For both deterministic and Monte Carlo simulations, the ad-  
joint flux is computed on the same 281-group SHEM energy grid (Hfaiedh and  
Santamarina, 2005). For the Monte Carlo simulation a cycle length of  $M = 5$   
ensures convergence of the asymptotic neutron importance via IFP. For this test  
215 case  $5 \times 10^3$  neutrons and  $10^4$  cycles were chosen for statistical accuracy. To  
minimize the biases between TRIPOLI-4<sup>®</sup> and APOLL02 due to the deterministic  
calculation options, the Monte Carlo simulation was performed in a multi-group  
mode. The adjoint flux  $\varphi^\dagger(E)$  was calculated averaging out  $\mathbf{r}$  and  $\mathbf{\Omega}$ <sup>5</sup>. A good  
agreement has been found on the whole energy range. The reduced  $\chi^2$  test yields  
220  $\chi^2 \simeq 1.07$ .

---

<sup>5</sup>The angular adjoint flux was integrated over the solid angle and the whole pin-cell volume.

	Composition $\frac{10^{24}}{\text{cm}^3}$		Composition $\frac{10^{24}}{\text{cm}^3}$
<b>Coolant</b>			
$^{23}\text{Na}$	2.500000E-2		
<b>Cladding</b>			
$^{54}\text{Fe}$	3.38587E-3	$^{56}\text{Fe}$	5.31510E-2
$^{57}\text{Fe}$	1.22749E-3	$^{58}\text{Fe}$	1.63356E-4
$^{50}\text{Cr}$	7.12849E-4	$^{52}\text{Cr}$	1.37466E-2
$^{53}\text{Cr}$	1.55875E-3	$^{54}\text{Cr}$	3.88007E-4
$^{58}\text{Ni}$	5.46116E-3	$^{60}\text{Ni}$	2.10362E-3
$^{61}\text{Ni}$	9.14511E-5	$^{62}\text{Ni}$	2.91521E-4
$^{64}\text{Ni}$	7.42840E-5	$^{55}\text{Mn}$	1.21336E-3
$^{59}\text{Co}$	1.10738E-4		
<b>Fuel</b>			
$^{235}\text{U}$	4.7803052E-05	$^{236}\text{U}$	3.9930001E-07
$^{238}\text{U}$	1.9522000E-02	$^{238}\text{Pu}$	4.0817999E-05
$^{239}\text{Pu}$	1.8232000E-03	$^{240}\text{Pu}$	7.7093998E-04
$^{241}\text{Pu}$	1.9767199E-04	$^{242}\text{Pu}$	1.6626000E-04
$^{241}\text{Am}$	1.4628800E-04	$^{237}\text{Np}$	1.4482600E-06
$^{16}\text{O}$	4.5940999E-02		

Table 3: Material compositions of the sodium-cooled MOX-pin-cell shown in Fig. 7.

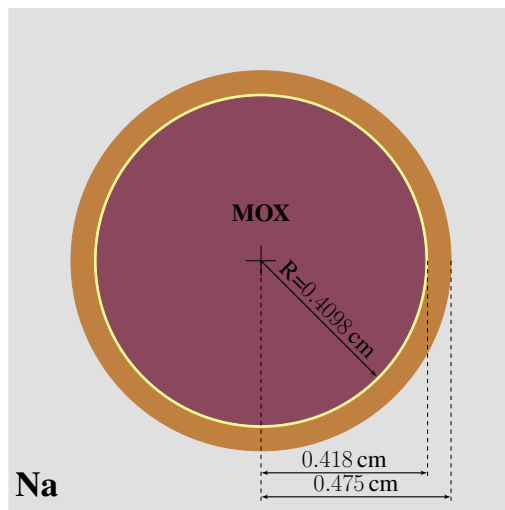


Figure 7: Sodium cooled MOX-pin-cell geometry.

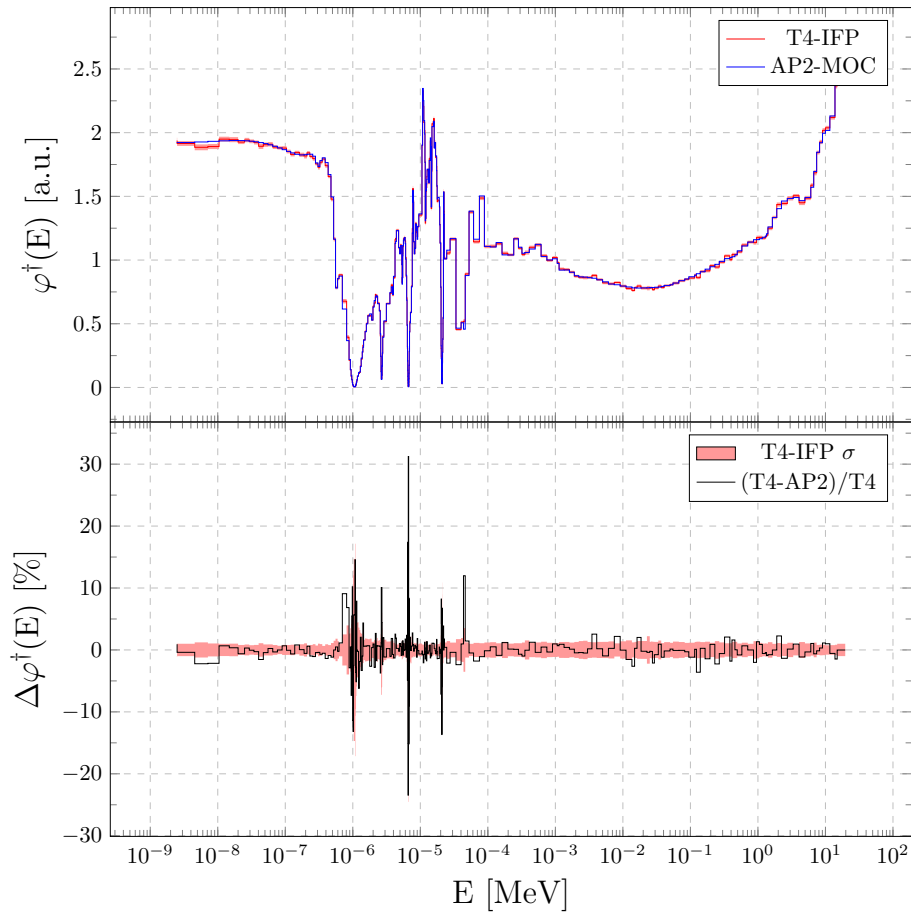


Figure 8: Comparison between TRIPOLI-4<sup>®</sup> and APOLL02 adjoint flux calculations for a sodium-cooled MOX-pin-cell (top). Relative differences between TRIPOLI-4<sup>®</sup> and APOLL02 are checked against the Monte Carlo error bars (bottom). The filled red band represents the TRIPOLI-4<sup>®</sup>  $1\sigma$ -statistical error.

### 4.3. UOX and MOX fuel assemblies

In order to further substantiate our analysis, we have finally considered UOX and MOX fuel assemblies representative of PWR reactors. The fuel rods are arranged in a  $17 \times 17$  square lattice with a pitch of 1.262082 cm. Additionally, 25 water holes are located as shown in Fig. 9, while fuel rod and water channel dimensions are provided in Tab. 4, where the radial mesh of the fuel pins used in the APOLLO2 calculations is also provided.

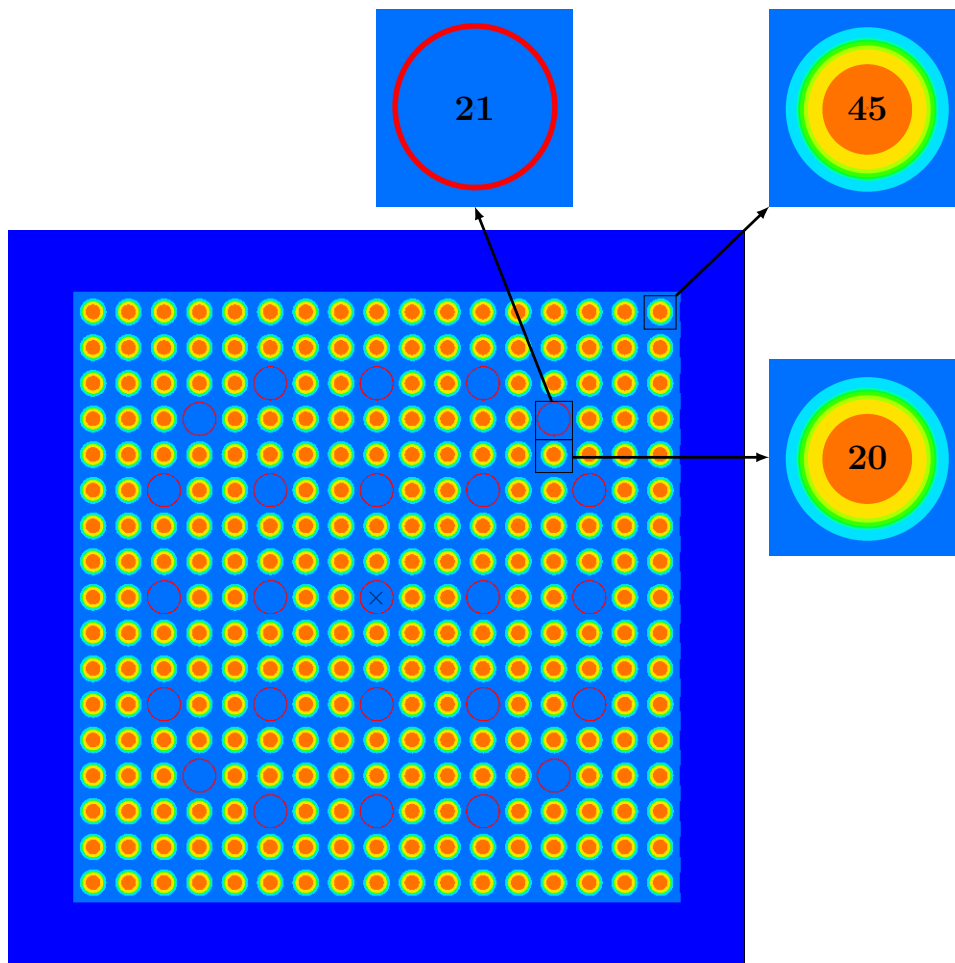


Figure 9: PWR  $17 \times 17$  fuel assembly configuration. The numbering associated to the fuel pin considered in the TRIPOLI-4<sup>®</sup>-APOLLO2 comparisons is shown.

MOX and UOX assemblies geometrical specifications are the same, only fuel material compositions differ. Fuel, cladding and coolant compositions for both assemblies are provided in Tab. 5.

Parameter	l [cm]	Parameter	l [cm]
<b>Fuel Rod</b>			
$R_1$	0.26099	$R_2$	0.34536
$R_3$	0.36909	$R_4$	0.39148
$R_5$	0.40221	$R_6$	0.41266
$G$	0.47436	$d$	1.262082
<b>Water Channel</b>			
$R_i$	0.56343	$R_e$	0.6035

Table 4: Fuel rod and water holes dimensions referring to parameters given in Fig. 10. Internal radius of the spatial mesh for the fuel pin used in APOLL02 is also given.

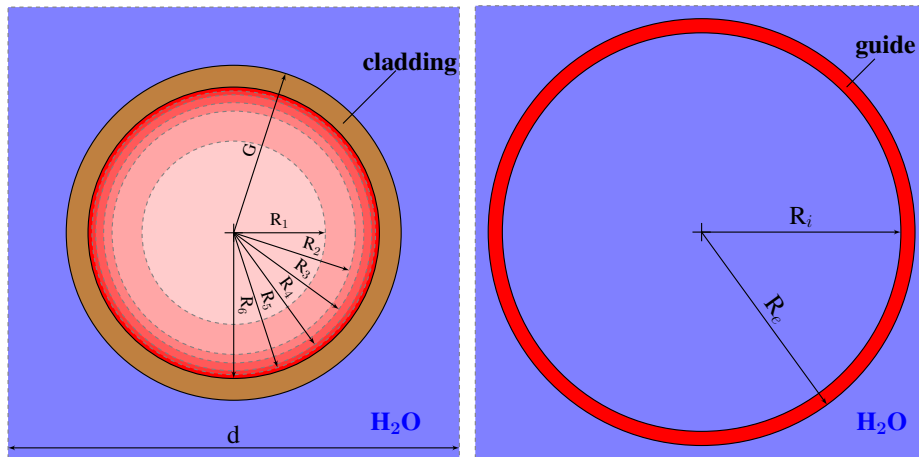


Figure 10: Fuel pin-cell and water channel guide tube dimensions. The values are provided in Tab. 4

	Composition $\frac{10^{24}}{\text{cm}^3}$		Composition $\frac{10^{24}}{\text{cm}^3}$
<b>Coolant at 574 K</b>			
$^1\text{H}$	4.771600E-2	$^{10}\text{B}$	3.972400E-6
$^{11}\text{B}$	1.589000E-5	$^{16}\text{O}$	2.385800E-2
<b>Water Channel Guide at 574 K</b>			
$^{54}\text{Fe}$	8.626900E-6	$^{56}\text{Fe}$	1.354200E-4
$^{57}\text{Fe}$	3.127500E-6	$^{58}\text{Fe}$	4.162200E-7
$^{50}\text{Cr}$	3.279900E-6	$^{52}\text{Cr}$	6.324900E-5
$^{53}\text{Cr}$	7.172000E-6	$^{54}\text{Cr}$	1.785300E-6
$^{16}\text{O}$	3.067400E-4	$^{90}\text{Zr}$	2.171980E-2
$^{91}\text{Zr}$	4.736510E-3	$^{92}\text{Zr}$	7.239810E-3
$^{94}\text{Zr}$	7.336880E-3	$^{96}\text{Zr}$	1.181990E-3
<b>Fuel UOX at 924 K</b>			
$^{235}\text{U}$	8.414800E-4	$^{238}\text{U}$	2.162500E-2
$^{16}\text{O}$	4.493200E-2		
<b>Fuel MOX at 924 K</b>			
$^{234}\text{U}$	3.939000E-7	$^{235}\text{U}$	4.952400E-5
$^{238}\text{U}$	2.168300E-2	$^{238}\text{Pu}$	2.224300E-5
$^{239}\text{Pu}$	7.016400E-4	$^{240}\text{Pu}$	2.713800E-4
$^{241}\text{Pu}$	1.328500E-4	$^{242}\text{Pu}$	6.698400E-5
$^{241}\text{Am}$	1.297800E-5	$^{242m}\text{Am}$	2.25690E-10
$^{16}\text{O}$	4.588200E-2		
<b>Fuel Cladding at 624 K</b>			
$^{90}\text{Zr}$	2.206000E-2	$^{91}\text{Zr}$	4.810700E-3
$^{92}\text{Zr}$	7.353200E-3	$^{94}\text{Zr}$	7.451800E-3
$^{96}\text{Zr}$	1.200500E-3		

Table 5: Material compositions of the UOX and MOX PWR assembly materials.

235 The APOLL02-code with a P5 anisotropy and 281 groups has been used to calculate the deterministic adjoint flux. The Method of Characteristic made available in APOLL02 has been chosen to solve the adjoint transport equation. The Livolant-Jeanpierre technique (Sanchez et al., 2010; Jeanpierre and Livolant, 1974) has been adopted to produce shelf-shielded cross sections. The Monte Carlo adjoint flux has been obtained via the IFP method in a continuous energy simulation of  $5 \times 10^4$  neutrons using  $10^5$  batches, with an IFP cycle length of  $M = 12$ . The adjoint flux results averaged on the whole volume for the UOX and MOX fuels are given in Fig. 11 and 12, respectively.

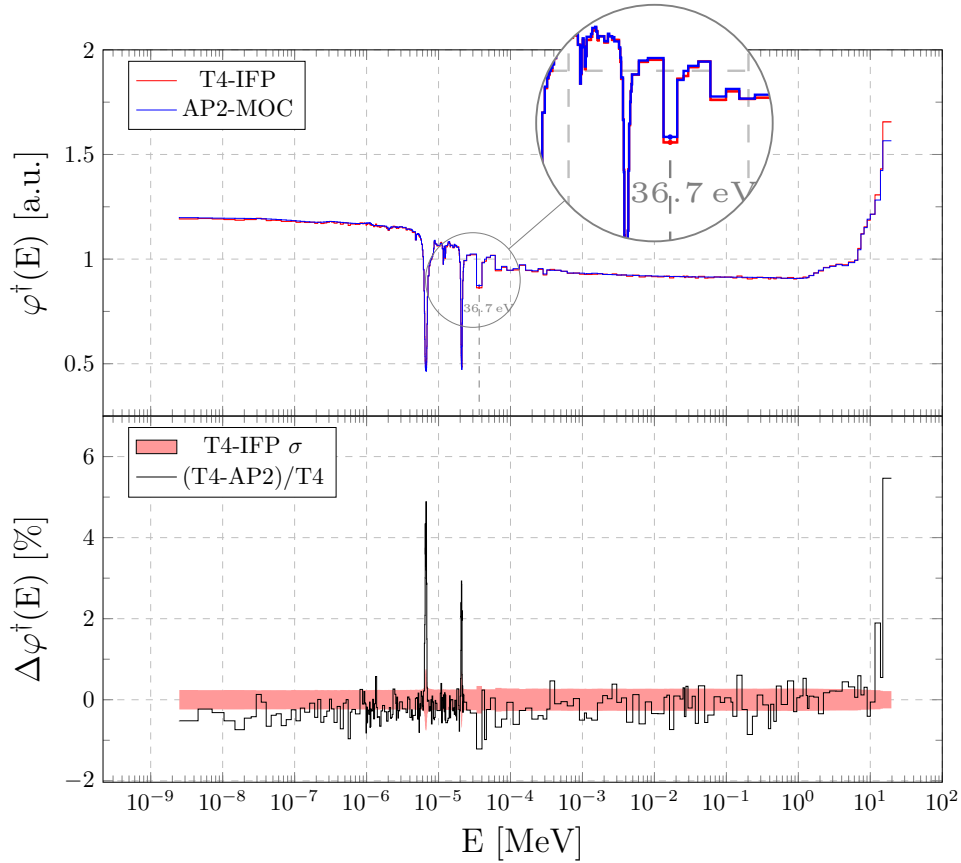


Figure 11: Comparison between TRIPOLI-4<sup>®</sup> and APOLL02 adjoint flux calculations for the PWR assembly with UOX fuel (top). Relative differences between TRIPOLI-4<sup>®</sup> and APOLL02 are checked against the Monte Carlo error bars (bottom). The filled red band represents the TRIPOLI-4<sup>®</sup>  $1\sigma$ -statistical error.

240 The  $\chi^2$  was estimated, yielding a value of  $\chi^2 \simeq 6.2$  for the PWR-UOX assem-

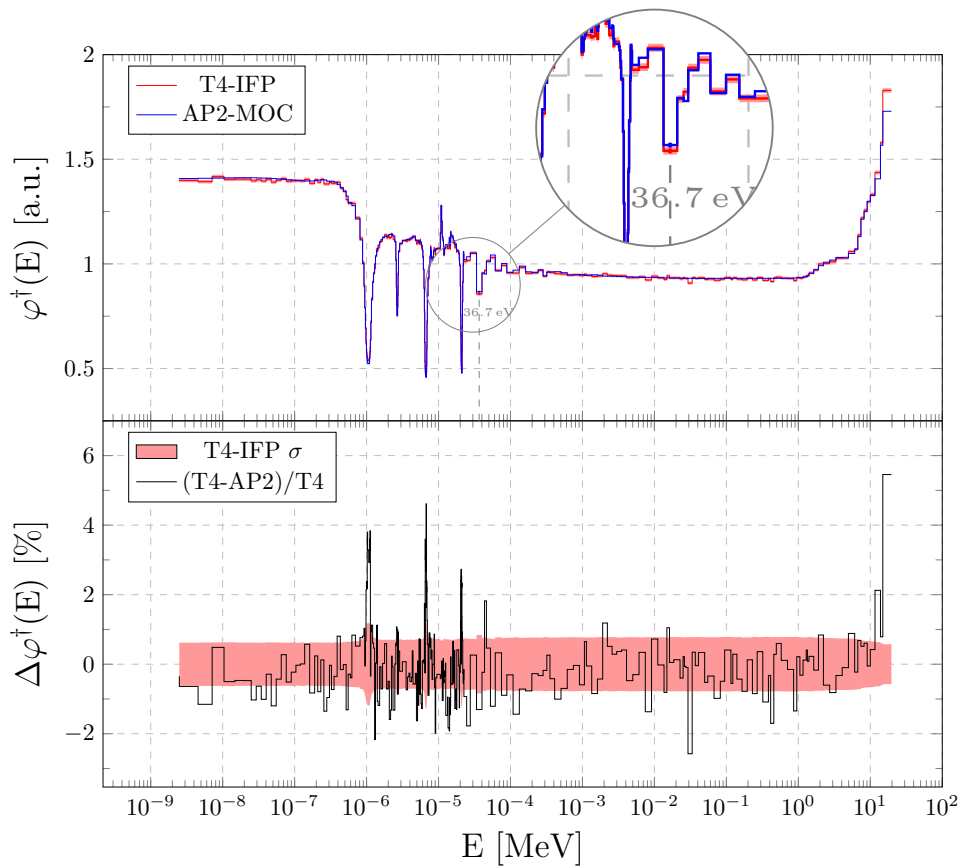


Figure 12: Comparison between TRIPOLI-4<sup>®</sup> and APOLLO2 adjoint flux calculations for the PWR assembly with MOX fuel (top). Relative differences between TRIPOLI-4<sup>®</sup> and APOLLO2 are checked against the Monte Carlo error bars (bottom). The filled red band represents the TRIPOLI-4<sup>®</sup>  $1\sigma$ -statistical error.

bly and  $\chi^2 \approx 1.9$  for the PWR-MOX assembly. Slight differences were detected between the deterministic and the Monte Carlo calculations, especially in the resonance energy region (see Figs. 11 and 12). This might probably be due to the multi-group approximation in the deterministic calculations. In particular, 245 the same discrepancy was observed in both cases close to the  $^{238}\text{U}$  resonance at 36.7 eV, where the chosen 281-group energy mesh is actually coarser. Even if the deterministic calculation options were chosen to achieve the best performance possible, self-shielding was based on the forward flux, providing the same cross sections to both adjoint and forward transport equations.

250 A more significant discrepancy was observed in the fast region, i.e.,  $E > 10$  MeV. The fastest energy group flux shows a discrepancy between the two calculations, presenting a relative difference of about 5%. This discrepancy manifests itself also in direct criticality calculations, so that we suspect that this issue might be due to the fact that the energy grid for the deterministic solver is not 255 fine enough in this region.

Another source of possible discrepancies between TRIPOLI-4<sup>®</sup> and APOLL02 calculations lies in the fact that TRIPOLI-4<sup>®</sup> uses evaluated cross section data at the temperatures given in Tab. 5, whereas for heavy nuclei and Zirconium APOLL02 will interpolate the data for 650 C between library tabulated values at 260 500 and 700 C. The moderator temperature, on the contrary, coincides with a tabulated value for the APOLL02 library.

## 5. Local adjoint flux calculations in UOX and MOX assemblies

The previous calculations showed a satisfactory comparison between TRIPOLI-4<sup>®</sup> and APOLL02 for the adjoint flux averaged over the angle and the entire assembly volume. Extended simulations were performed in order to verify whether 265 local adjoint fluxes in the fuel and in the coolant do provide comparable results between the two codes, running  $10^5$  neutrons for  $5 \times 10^4$  batches in the Monte Carlo simulations.

In Figs. 13, 14, 15 and 16 we illustrate the adjoint flux in the fuel pin number 270 20 and 45<sup>6</sup> for both UOX and MOX assemblies, respectively (see Fig. 9 for fuel pin numbering). The same discrepancies observed in the whole assembly calculations are now more apparent for both fuel kinds and for both pin cells, regardless of their location in the assembly lattice. The adjoint flux calculation for the pin-cell number 20 yields results similar to those obtained for pin-cell

---

<sup>6</sup>The angular adjoint flux was integrated over the solid angle and the fuel pin-cell volume (excluding cladding).

275 45, although the former is closer to the water hole and the latter is located in a peripheral and less moderated region. This is confirmed by the  $\chi^2$  results given in Tab. 6.

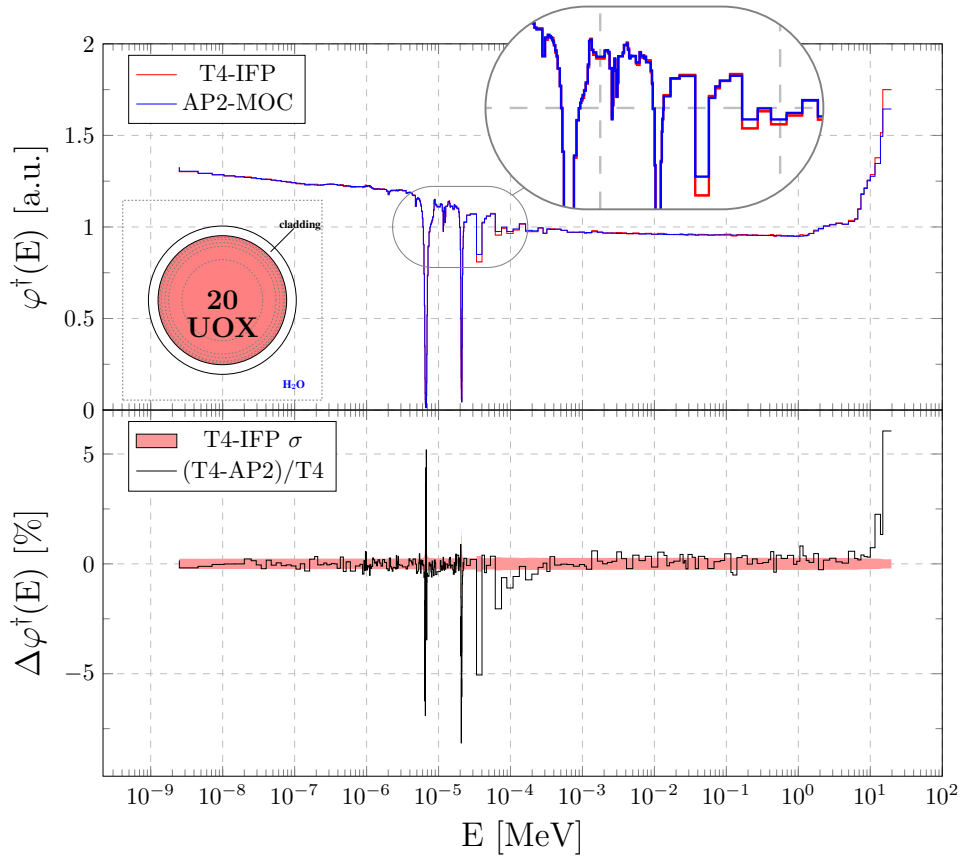


Figure 13: Comparison between TRIPOLI-4<sup>®</sup> and APOLL02 adjoint flux calculations for the PWR assembly with UOX fuel, in the whole fuel pin number 20 (top). Relative differences between TRIPOLI-4<sup>®</sup> and APOLL02 are checked against the Monte Carlo error bars (bottom). The filled red band represents the TRIPOLI-4<sup>®</sup>  $1\sigma$ -statistical error. The coloured region in the fuel pin picture represents the volume over which the flux has been integrated.

280 In order to better apprehend at which spatial location within the pin-cell the discrepancy between the adjoint flux of TRIPOLI-4<sup>®</sup> and APOLL02 increases, several simulations were performed so as to estimate the adjoint flux integrated over different cylindrical shells in the fuel pin of the UOX fuel assembly. In Figs. 17 and 18 the adjoint flux in the most external cylindrical shell of the fuel pin number 20 is presented for both UOX and MOX assemblies, respectively (see Fig. 9 for fuel pin numbering). Although for higher energies the discrepancies ob-

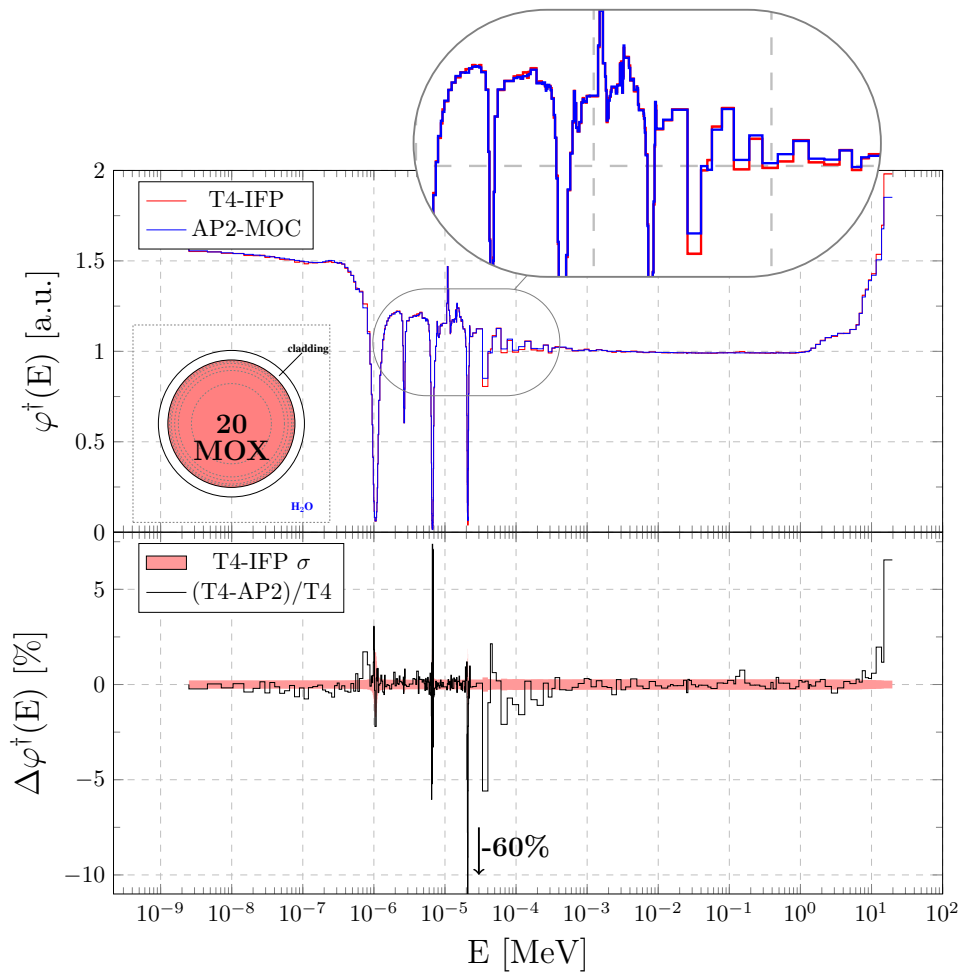


Figure 14: Comparison between TRIPOLI-4<sup>®</sup> and APOLL02 adjoint flux calculations for the PWR assembly with MOX fuel, in the whole fuel pin number 20 (top). Relative differences between TRIPOLI-4<sup>®</sup> and APOLL02 are checked against the Monte Carlo error bars (bottom). The filled red band represents the TRIPOLI-4<sup>®</sup>  $1\sigma$ -statistical error. The coloured region in the fuel pin picture represents the volume over which the flux has been integrated.

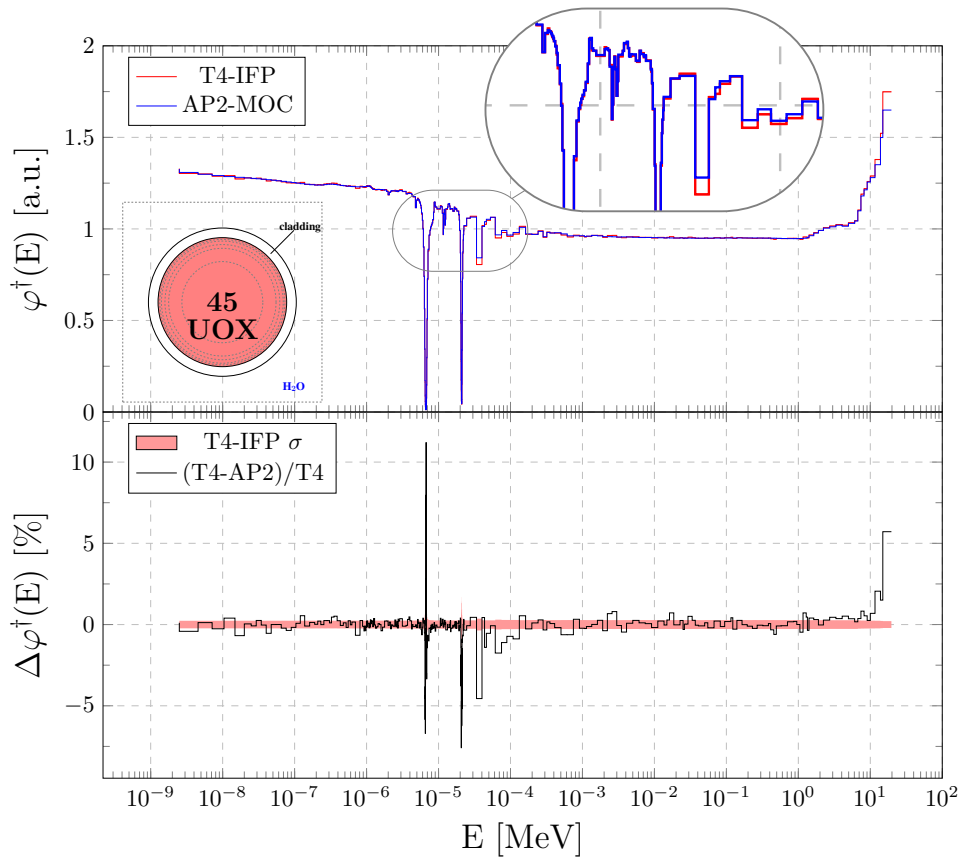


Figure 15: Comparison between TRIPOLI-4<sup>®</sup> and APOLL02 adjoint flux calculations for the PWR assembly with UOX fuel, in the whole fuel pin number 45 (top). Relative differences between TRIPOLI-4<sup>®</sup> and APOLL02 are checked against the Monte Carlo error bars (bottom). The filled red band represents the TRIPOLI-4<sup>®</sup>  $1\sigma$ -statistical error. The coloured region in the fuel pin picture represents the volume over which the flux has been integrated.

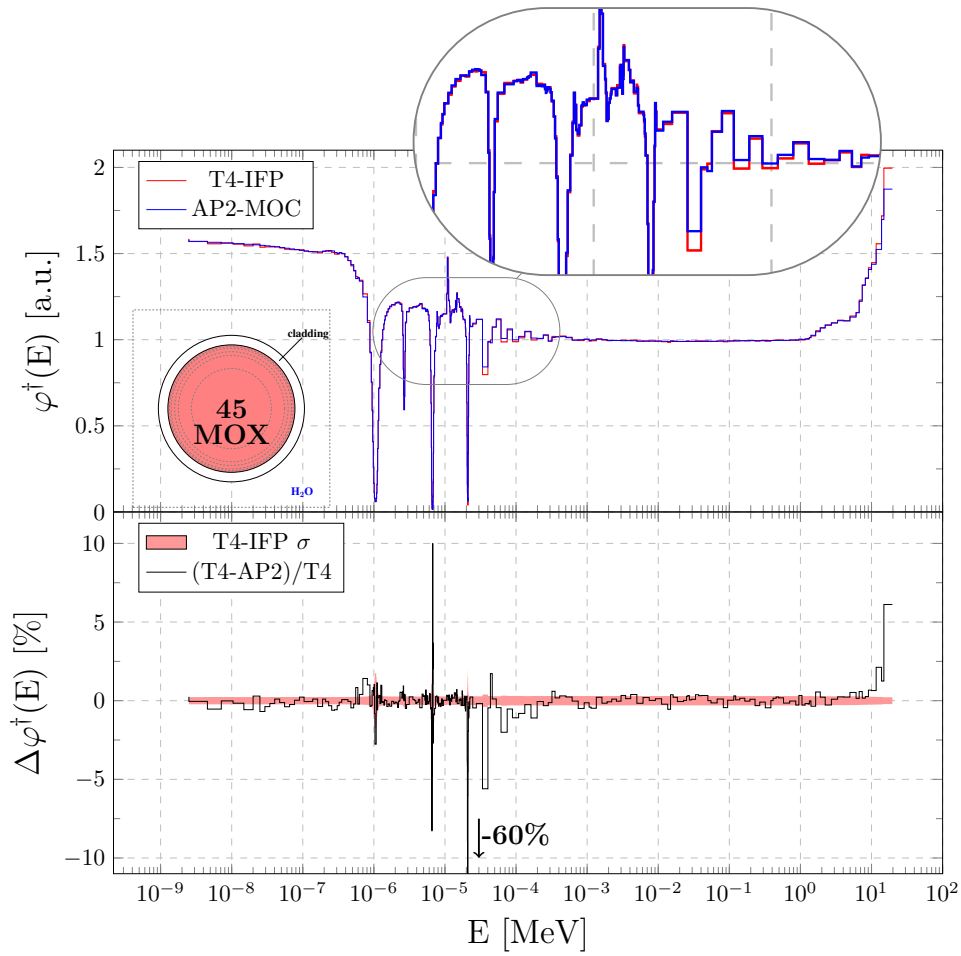


Figure 16: Comparison between TRIPOLI-4<sup>®</sup> and APOLL02 adjoint flux calculations for the PWR assembly with MOX fuel, in the whole fuel pin number 45 (top). Relative differences between TRIPOLI-4<sup>®</sup> and APOLL02 are checked against the Monte Carlo error bars (bottom). The filled red band represents the TRIPOLI-4<sup>®</sup>  $1\sigma$ -statistical error. The coloured region in the fuel pin picture represents the volume over which the flux has been integrated.

285 served for pin-cell calculations look the same as for the whole assembly, a clear improvement in the energy region corresponding to the resonance at 36.7 eV is observed.

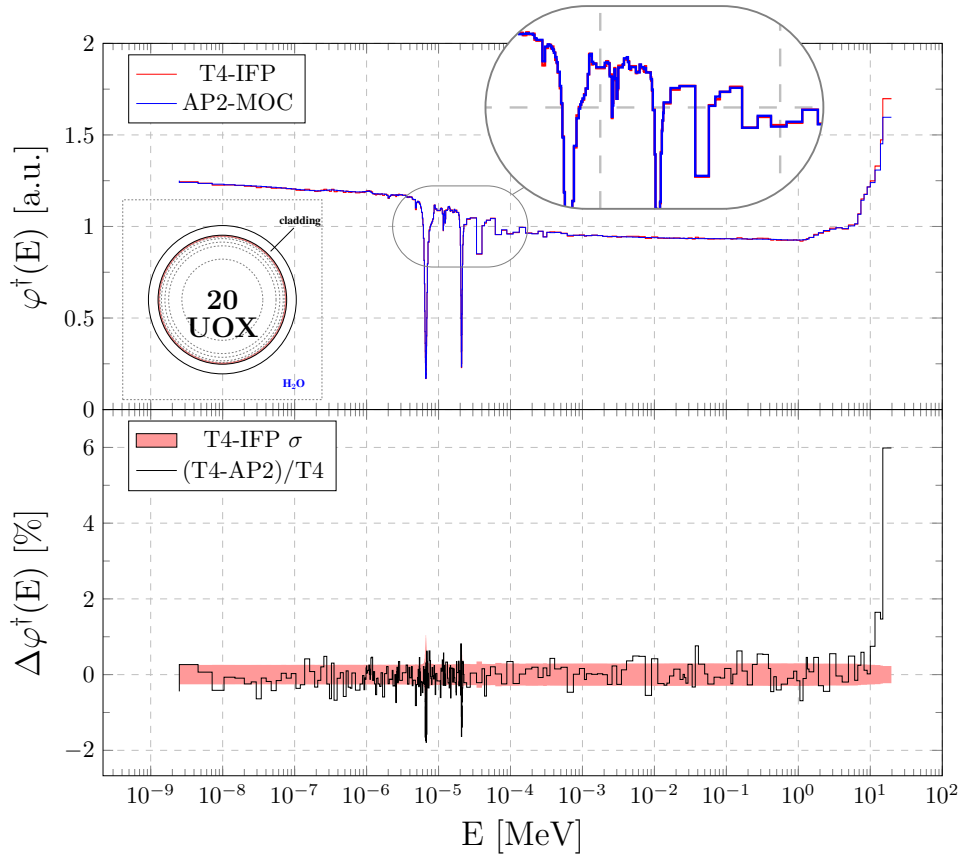


Figure 17: Comparison between TRIPOLI-4<sup>®</sup> and APOLL02 adjoint flux calculations for the PWR assembly with UOX fuel, in the most external fuel pin cylindrical shell (top). Relative differences between TRIPOLI-4<sup>®</sup> and APOLL02 are checked against the Monte Carlo error bars (bottom). The filled red band represents the TRIPOLI-4<sup>®</sup>  $1\sigma$ -statistical error. The coloured region in the fuel pin picture represents the volume over which the flux has been integrated.

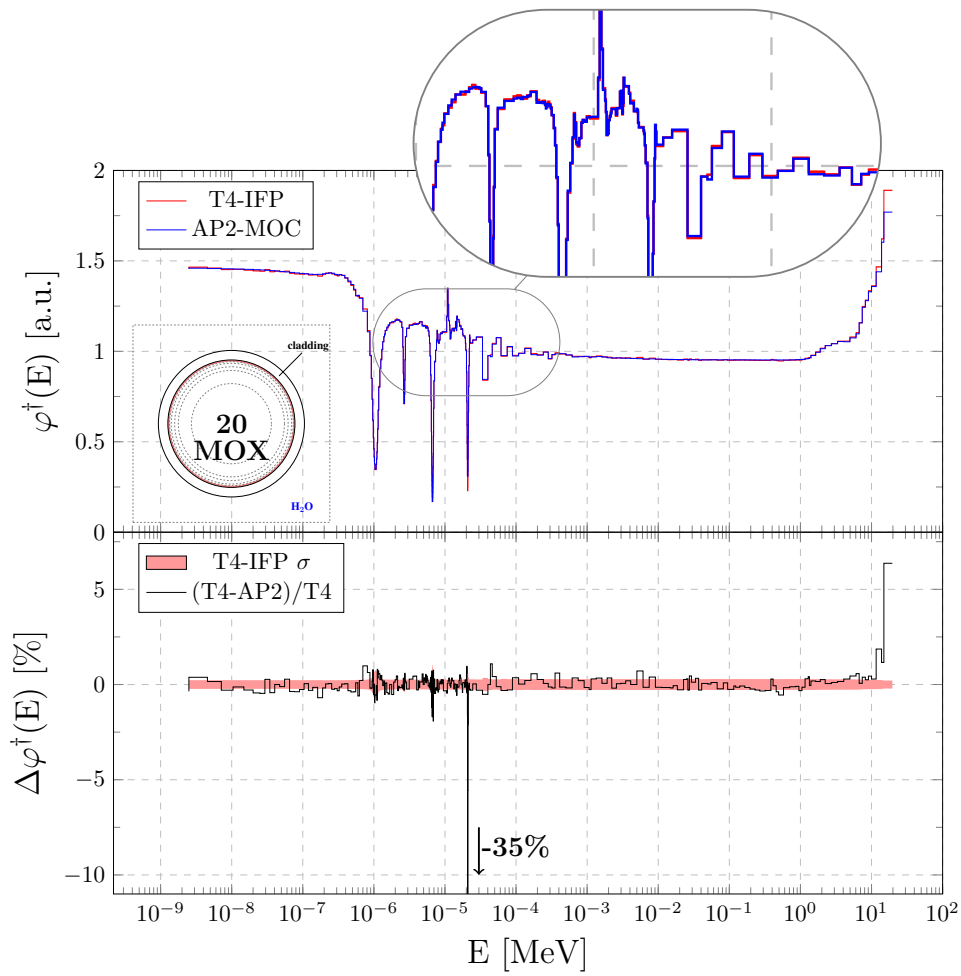


Figure 18: Comparison between TRIPOLI-4<sup>®</sup> and APOLL02 adjoint flux calculations for the PWR assembly with MOX fuel, in the most external fuel pin cylindrical shell (top). Relative differences between TRIPOLI-4<sup>®</sup> and APOLL02 are checked against the Monte Carlo error bars (bottom). The filled red band represents the TRIPOLI-4<sup>®</sup>  $1\sigma$ -statistical error. The coloured region in the fuel pin picture represents the volume over which the flux has been integrated.

Fig. 19 shows how the discrepancies between deterministic and Monte Carlo calculations increase when moving from the periphery to the center in the cylindrical shells of the fuel pin number 20. In the central region of the fuel a discrepancy is observed between APOLLO2 and TRIPOLI-4<sup>®</sup>, which is also apparent in the  $\chi^2$  values reported in Tab. 6. This might be due to the fact that neutrons born in the central region of the pin-cell have a smaller probability to leave the fuel. In particular, those born with an energy close to the resonance at 36.7 eV have a significant probability to be promptly absorbed, yielding a lower value for the adjoint flux. Otherwise, neutrons in the peripheral region of the pin-cell have a larger probability to scatter outside in the cladding or in the coolant, even close to 36.7 eV. The resonance region strongly affects the calculation of the adjoint flux in the central volume of the fuel pins, which justifies the noticeable discrepancies due to preparing adjoint self-shielded cross sections by using the forward flux in the deterministic calculations. Actually, the self-shielding formalism of APOLLO2 is based on a forward slowing-down problem, while accounting for spatial effects using the collision probability approximation, which assumes isotropic emission sources. This might explain the discrepancies of the adjoint flux in the internal fuel regions close to the resonance energies.

The same analysis has been performed for the water hole number 21, whose  $\chi^2$  values are provided in Tab. 6. Simulation results are illustrated in Figs. 20 and 21 for UOX and MOX fuels, respectively. In water, calculating the adjoint flux in the resonance energy domain does not show any significant issue: discrepancies are all included in the  $2\sigma$  Monte Carlo error bars. However, a systematic albeit slight difference was observed in the thermal energy domain, where the Monte Carlo adjoint flux appears to be underestimated if compared to the deterministic calculations.

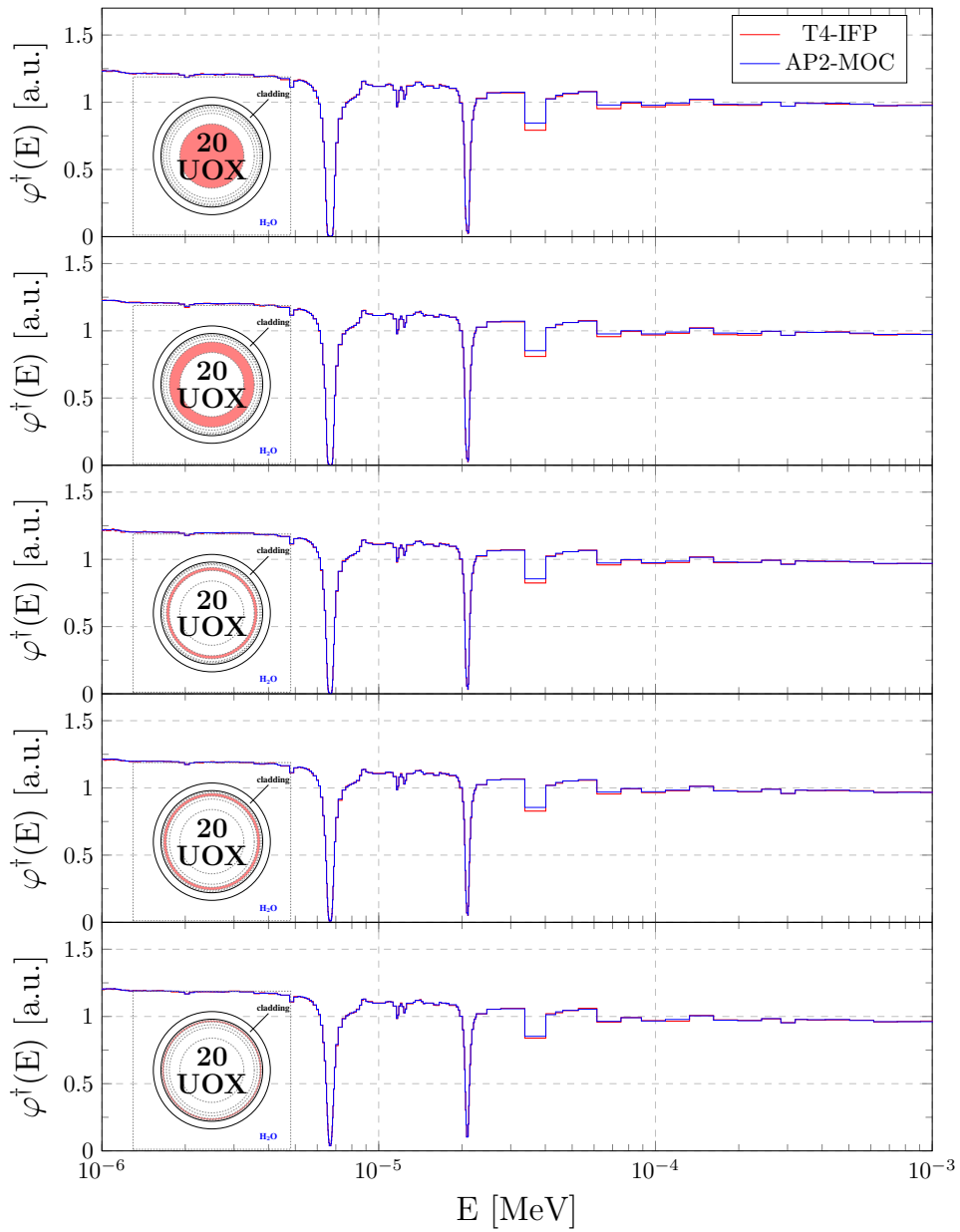


Figure 19: Comparison between TRIPOLI-4<sup>®</sup> and APOLL02 adjoint flux calculations for the PWR assembly with UOX fuel, in the fuel pin number 20 and in different cylindrical shells. The coloured red region in the fuel pin picture represents the volume over which the flux has been integrated.

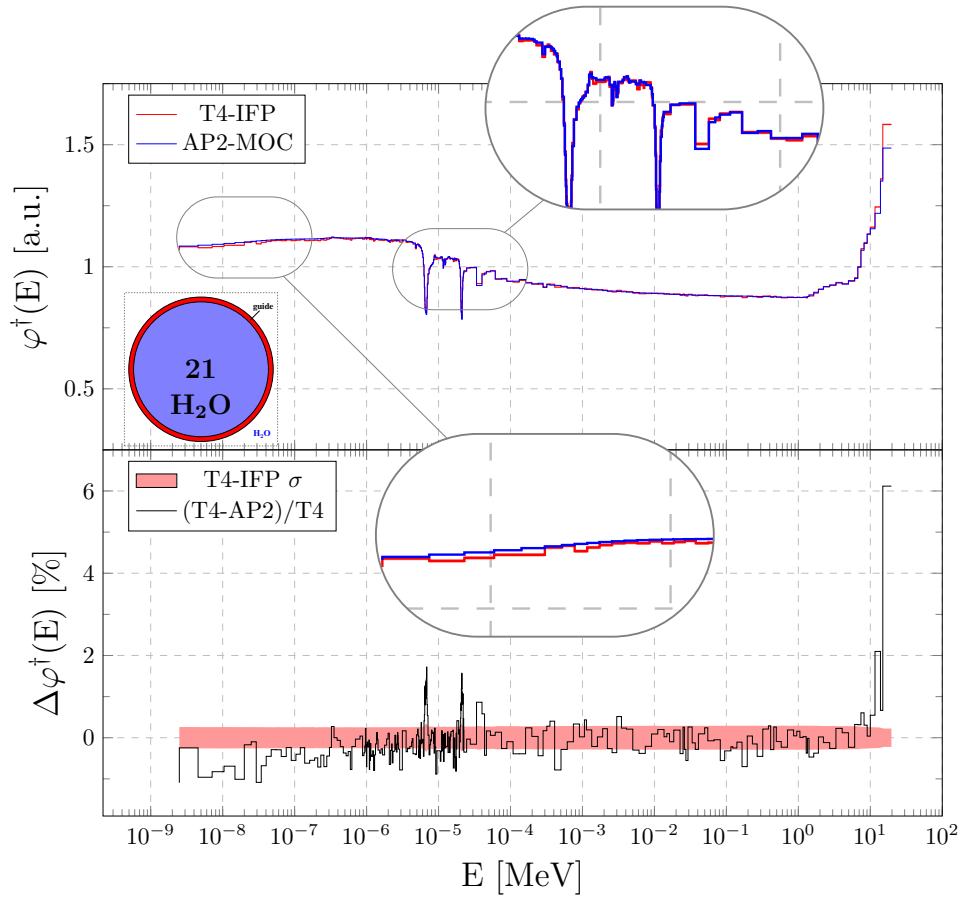


Figure 20: Comparison between TRIPOLI-4<sup>®</sup> and APOLL02 adjoint flux calculations for the PWR assembly with UOX fuel, in the water hole number 21 (top). Relative differences between TRIPOLI-4<sup>®</sup> and APOLL02 are checked against the Monte Carlo error bars (bottom). The filled red band represents the TRIPOLI-4<sup>®</sup>  $1\sigma$ -statistical error. The coloured region in the fuel pin picture represents the volume over which the flux has been integrated.

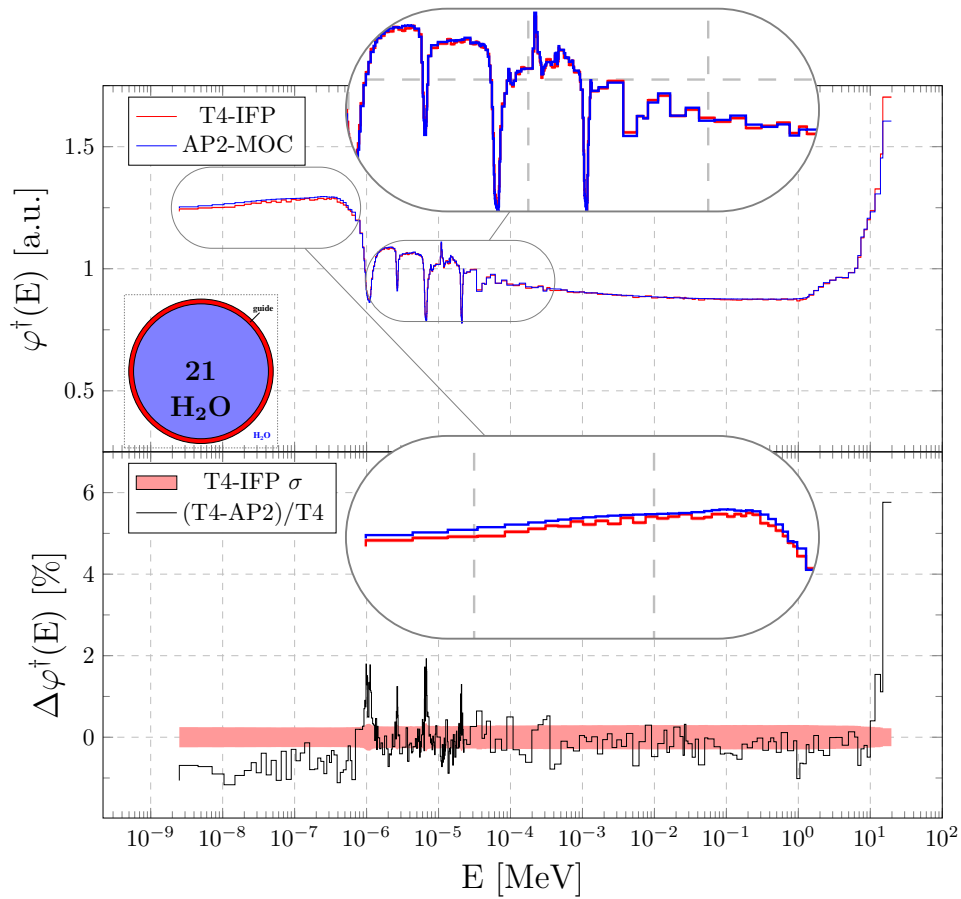


Figure 21: Comparison between TRIPOLI-4<sup>®</sup> and APOLL02 adjoint flux calculations for the PWR assembly with MOX fuel, in the water hole number 21 (top). Relative differences between TRIPOLI-4<sup>®</sup> and APOLL02 are checked against the Monte Carlo error bars (bottom). The filled red band represents the TRIPOLI-4<sup>®</sup> 1 $\sigma$ -statistical error. The coloured region in the fuel pin picture represents the volume over which the flux has been integrated.

	$\chi^2$		$\chi^2$
<b>UOX fuel</b>			
Whole Assembly	6.2	Fuel pin 20	6.5
Fuel pin 45	6.2	Fuel pin 20 C <sub>1</sub>	12.0
Fuel pin 20 C <sub>2</sub>	8.6	Fuel pin 20 C <sub>3</sub>	5.7
Fuel pin 20 C <sub>4</sub>	4.4	Fuel pin 20 C <sub>5</sub>	4.3
Fuel pin 20 C <sub>6</sub>	3.9	Water hole 21	5.9
<b>MOX fuel</b>			
Whole Assembly	1.9	Fuel pin 20	16.7
Fuel pin 45	14.2	Fuel pin 20 C <sub>6</sub>	15.7
Water hole 21	6.8		

Table 6:  $\chi^2$  results for assembly adjoint flux calculations. The C<sub>*i*</sub> refers to the different cylindrical shells of the fuel pin for APOLLO2 calculations.

Forward flux calculations were also performed in order to verify whether the  
315 observed differences between APOLLO2 and TRIPOLI-4<sup>®</sup> for the adjoint flux pro-  
files were comparable to those obtained in direct eigenvalue calculations. Track  
scores were collected by simulating 10<sup>5</sup> neutrons in 10<sup>5</sup> cycles with TRIPOLI-  
4<sup>®</sup> to estimate the forward flux in the different cylindrical shells of the fuel  
pin number 20. A comparison between the Monte Carlo and the deterministic  
320 calculations for the inner cylindrical region is shown in Fig. 22. Some discrepan-  
cies were observed, which led a  $\chi^2 = 783$ , much higher than what we observed  
for the adjoint calculations. Large values of  $\chi^2$  might be probably due to the  
small statistical uncertainty obtained in the Monte Carlo simulations: however,  
these differences clearly show that for the adjoint problem most discrepancies  
325 are induced by the neutron transport simulation. The Monte Carlo IFP algorithm  
implemented in TRIPOLI-4<sup>®</sup> can be then considered as reference tool for adjoint  
calculations.

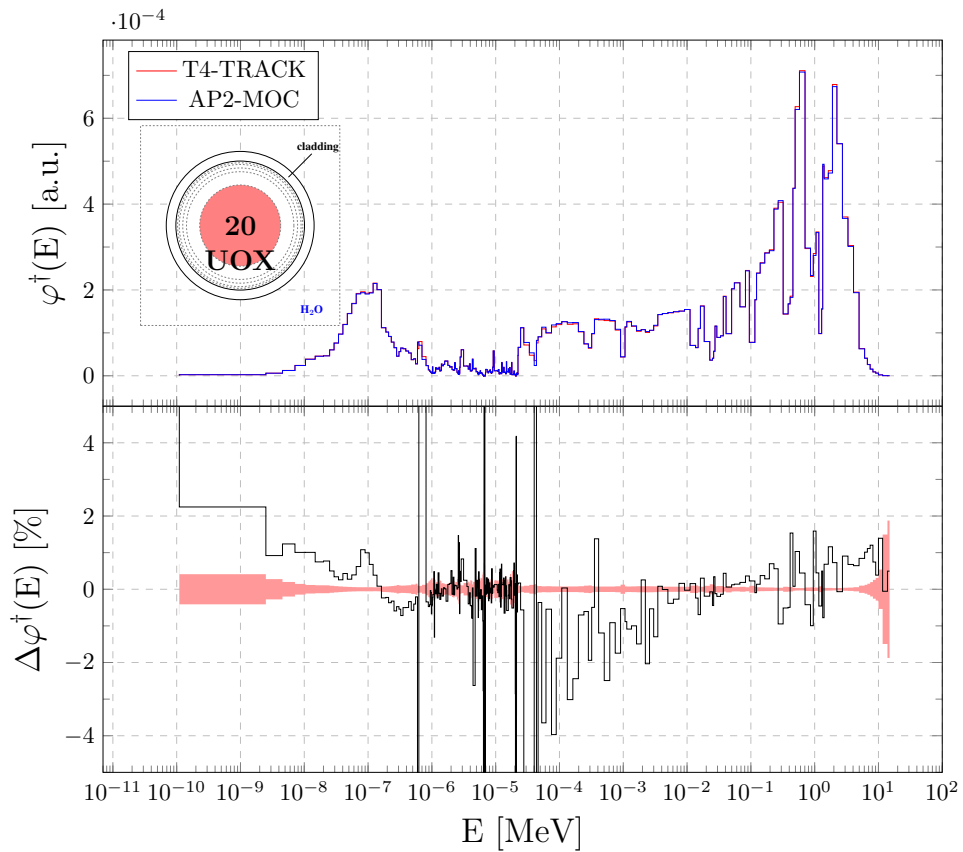


Figure 22: Comparison between TRIPOLI-4<sup>®</sup> and APOLL02 forward flux calculations for the PWR assembly with UOX fuel, in the inner region of the pin-cell number 20 (top). Relative differences between TRIPOLI-4<sup>®</sup> and APOLL02 are checked against the Monte Carlo error bars (bottom). The filled red band represents the TRIPOLI-4<sup>®</sup>  $1\sigma$ -statistical error. The coloured region in the fuel pin picture represents the volume over which the flux has been integrated.

## 6. Comparing forward and adjoint flux calculations

Direct and adjoint criticality calculations correspond to intrinsically different simulation strategies, the former being based on the power iteration for the eigenvalue form of the Boltzmann equation, and the latter being based on a special formulation of a fixed source transport problem. It is nonetheless interesting to compare the two approaches, which can provide complementary pieces of information concerning multiplying systems. We conclude thus our analysis of the adjoint flux calculations made available in TRIPOLI-4<sup>®</sup> by considering the performance of such algorithms. Direct and forward flux calculations based on a 281-group mesh (see Fig. 23) were run for MOX fuel pin-cell (examined in Sec. 4.2) on 10 Intel<sup>®</sup> Xenon<sup>®</sup> CPUs E5-2620 at 2.0 GHz.

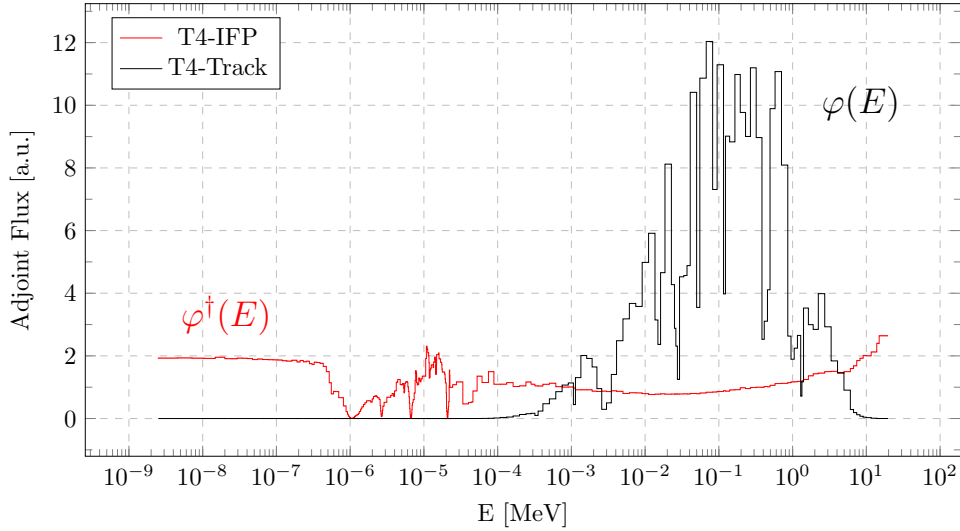


Figure 23: Adjoint (IFP) and forward (track estimator) flux calculations for a sodium cooled MOX-pin-cell.

Concerning the simulation options,  $5 \times 10^3$  neutrons were simulated in  $10^4$  cycles in both cases. The number of latent generations for the IFP calculation was set to  $M = 12$ . To compare the performances of the two calculations, the Figure of Merit (FOM) parameter

$$\text{FOM} = \frac{1.0}{\sigma^2 T} \quad (25)$$

was estimated, where  $T$  is the computer time and  $\sigma^2$  the variance of the Monte Carlo score. For  $\sigma$  we choose the standard deviation of the adjoint and forward

345 flux norms, obtained by quadratic sums of the single group flux values<sup>7</sup>. The direct calculation shows better performances: it is slower than the adjoint calculation, but yields smaller statistical uncertainties. The ratio between the two FOMs turns out to be in fact

$$\left( \frac{\text{FOM}_\varphi}{\text{FOM}_{\varphi^\dagger}} \right)_{\text{cell}} = 137, \quad (26)$$

which clearly shows higher efficiency performing the forward flux calculation.

350 The same performance indicator was used for an assembly simulation with UOX fuel. The adjoint and the forward 281-group flux have been computed on the whole assembly volume, averaging out the  $\mathbf{r}$  and  $\mathbf{\Omega}$  coordinates (see Fig. 24).  $5 \times 10^4$  neutrons were simulated for  $10^5$  cycles on 100 Xeon E5-2680 V2 CPUs at 2.8 GHz. Although the adjoint calculation was faster than the forward one, the ratio between the two FOMs turns out to be

$$\left( \frac{\text{FOM}_\varphi}{\text{FOM}_{\varphi^\dagger}} \right)_{\text{assembly}} = 594. \quad (27)$$

Not surprisingly, the IFP algorithm demands non-negligible computational efforts in terms of CPU-time when compared to direct criticality calculations. Nevertheless, adjoint criticality simulations are a powerful tool for the verification of deterministic codes and for the physical analysis of reactor configurations, as a complement of standard direct simulations. Moreover, it should be stressed that adjoint calculations can easily estimate point-flux contributions at a given location in the phase space, a task which is prohibitively expensive for direct simulations.

## 7. Conclusions

365 In this paper we have illustrated the implementation and the verification tests of the adjoint flux calculation capability in the Monte Carlo code TRIPOLI-4<sup>®</sup>, in view of a future release. The basic IFP algorithm has been first briefly recalled, for the sake of completeness. We have then shown the adjoint flux profiles obtained with TRIPOLI-4<sup>®</sup> on some relevant reactor configurations, including a two-group infinite-medium model, mono-kinetic transport, sodium-cooled

---

<sup>7</sup>Both flux and standard deviation were renormalized to the same norm. The variance of the norm for the forward and the adjoint calculations was obtained by assuming that flux values at different energies are not correlated.

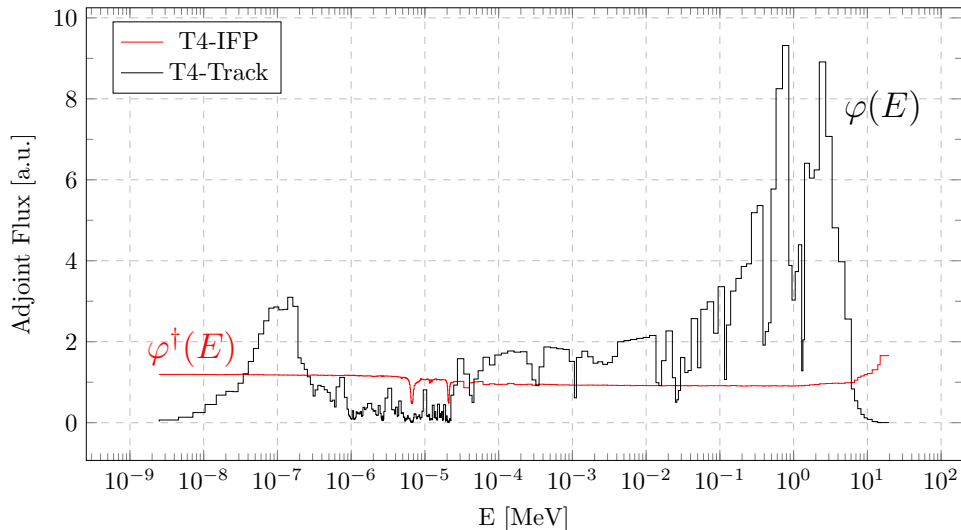


Figure 24: Adjoint (IFP) and forward (track estimator) flux calculations for a PWR assembly with UOX fuel.

fuel pin-cells and PWR assemblies in continuous-energy transport. For all tested configurations, the simulation results of TRIPOLI-4<sup>®</sup> have been compared to exact solutions (where available) and to the adjoint flux profiles obtained by resorting to the deterministic solvers APOLLO2 and ERANOS. A satisfactory agreement has been found. Nonetheless, for some configurations and energy ranges, slight discrepancies have been detected, which might come from the fact that the cross sections needed for self-shielding in the deterministic solvers have been computed by weighting by the direct neutron flux. Geometry and material specifications have been provided, in order for the reader to possibly reproduce our results and compare them to those of other deterministic solvers or Monte Carlo codes.

Special emphasis has been given to the analysis of benchmark-quality UOX and MOX assemblies, where the global and local (i.e., at the scale of a single pin-cell of the lattice) adjoint flux profiles have been computed and verified against those produced by APOLLO2. Comparison with respect to direct Monte Carlo criticality calculations has shown that the IFP method implies higher computational costs, which are balanced by the possibility of exploring a whole new domain of simulation for criticality problems (adjoint flux profiles basically inaccessible to Monte Carlo codes until the appearance of the IFP method). In this respect, a particularly attractive feature is the possibility of computing the adjoint flux in a single point of phase space.

Future research will be aimed at extending these comparisons to the case of

$\alpha$ -eigenfunction adjoint calculations, along the lines of the methods proposed in (Terranova and Zoia, 2017).

## Acknowledgements

395 TRIPOLI-4<sup>®</sup> is a registered trademark of CEA. The authors wish to thank  
Électricité de France (EDF) for partial financial support, and express their grati-  
tude to Dr. F. Malvagi of CEA/Saclay for fruitful discussions.

## References

- Bell, G. I., Glasstone, S., 1970. Nuclear reactor theory, Van Nostrand Reinhold Company.
- 400 Brun, E., et al., 2015. Ann. Nucl. Energy **82**, 151-160.
- Choi, S., H., Shim, H., J., 2016. Ann. Nucl. Energy **96**, 287.
- Cover, T., Thomas, J., 2006. Elements of information theory, Wiley-Interscience publication.
- Feghhi, S. A. H., Shahriari, M., Afarideh, H., 2007. Ann. Nucl. Energy **34**, 514.
- Feghhi, S. A. H., Shahriari, M., Afarideh, H., 2008. Ann. Nucl. Energy **35**, 1397.
- 405 Henry, A.F., 1975. Nuclear Reactor Analysis, The MIT Press.
- Hfaiedh, N., Santamarina, A., 2005. In *Proceedings of the MC 2015 conference*, Avignon, France.
- Hoogenboom, J. E., 2003. Nuc. Sci. Eng. **143**, 99.
- Hurwitz Jr., H., 1964. In: Radkowsky, A. (Ed.), Naval Reactors Physics Handbook, vol. I. Naval  
410 Reactors, Division of Reactor Development, United States Atomic Energy Commission, pp. 864.
- Kiedrowski, B.C., 2010. LA-UR-10-01803.
- Kiedrowski, B. C., 2011. *Adjoint Weighting for Continuous-Energy Monte Carlo Radiation Transport*, PhD thesis, Michigan University.
- 415 Kiedrowski, B. C., Brown, F. B., Wilson, P. P. H., 2011. Nucl. Sci. Eng. **68**, 226.
- Kiedrowski, B. C., Brown, F. B., 2013. Nucl. Sci. Eng. **174**, 227.
- Leppänen, J., et al., 2014. Ann. Nucl. Energy **65**, 272.
- Jeanpierre, F., Livolant, M., 1974. CEA Report 4533.
- Lux, I., Koblinger, L., 1991. Monte Carlo particle transport methods: Neutron and photon calcu-  
420 lations, CRC Press, Boca Raton.
- Mosteller, R. D., Kiedrowski, B. C., 2011. LA-UR-11-04409, Los Alamos National Laboratory.
- Nauchi, Y., Kameyama, T., 2010. J. Nucl. Sci. Technol. **47**, 977.
- Perfetti, C. M., 2012. *Advanced Monte Carlo methods for eigenvalue sensitivity coefficient cal-  
culations*, PhD thesis, Michigan University.
- 425 Palmiotti, G., Rieunier, J. M., Gho, C., Salvatores, M., 1990. Nucl. Sci. Eng. **104**, 26-33.
- Qiu, Y., Shang, X., Tang, X., Liang, J., Wang, K., 2016. Ann. Nucl. Energy **87**, 228.
- Ruggieri, J.-M., Tommasi, J., Lebrat, J.-F., Suteau, C., Plisson-Rieunier, D., De Saint Jean, C., Rimpault, G., Sublet, J.-C., 2006. In *Proceedings of the ICAPP2006 conference*, Reno, Nevada.
- 430 Sanchez, R., Mondot, J., Stankovski, Z., Cossic, A., Zmijarevic, I., 1988. Nucl. Sci. Eng. **100**, 352-362.

- Sanchez, R., Zmijarevic, I., Coste-Delclaux, M., Masiello, E., Santandera, S., Martinolli, E., Villate, L., Schwartz, N., Guler, N., 2010. Nucl. Eng. Techn. **42**, 474-499.
- Shannon, C., 1948. The Bell System Technical Journal **27**, 379-423.
- 435 Shim, H. J., Kim, C. H., Kim, Y., 2011. J. Nucl. Sci. Technol. **48**, 1453.
- Soodak, H., 1949. Pile kinetics. In: Goodman, G. (Ed.), The Science and Engineering of Nuclear Power, vol. II. Addison-Wesley Press, Inc., Cambridge, pp. 89102.
- Terranova, N., Zoia, A., 2017. Annals of Nuclear Energy **108**, 57-66.
- Truchet, G., et al., 2014. In *Proceedings of the SNA+MC 2013 conference*, Paris, France.
- 440 Truchet, G., et al., 2014. In *Proceedings of the Physor 2014 conference*, Kyoto, Japan.
- Truchet, G., 2015. *Développements et validation de calculs à énergie continue pondérés par l'importance*, PhD thesis, Grenoble Alpes University.
- Truchet, G., Leconte, P., Santamarina, A., Damian, F., Zoia, A., 2015. Ann. Nucl. Energy **81**, 17-26.
- 445 Ussachoff, L. N., 1955. In *Proceedings of the 1st UN conference of the peaceful uses of atomic energy*, P/503, Geneva, Switzerland.
- Weinberg, A.M., 1952. Am. J. Phys. **20**, 401-412.
- Zoia A., Brun, E., 2016. Annals of Nuclear Energy **90**, 71-82.
- Zoia, A., Nauchi, Y., Brun, E., Jouanne, C., 2016. Annals of Nuclear Energy **96**, 377-388.